Simulations and measurements of GaAs–based photoelectrochemical cells

Lassi Hällström

School of Electrical Engineering

Thesis submitted for examination for the degree of Master of Science in Technology.

Espoo 22.01.2018

Thesis supervisor:

Prof. Ilkka Tittonen

Thesis advisor:

M.Sc. Camilla Tossi

Aalto University
School of Electrical Engineering

AALTO UNIVERSITY
SCHOOL OF ELECTRICAL ENGINEERING

ABSTRACT OF THE
MASTER'S THESIS

Author: Lassi Hällström

Title: Simulations and measurements of GaAs–based photoelectrochemical cells

Date: 22.01.2018 Language: English Number of pages: 7+51

Department of Electronics and Nanoengineering

Professorship: S–129 Electrophysics

Supervisor: Prof. Ilkka Tittonen

Advisor: M.Sc. Camilla Tossi

The photoelectrochemical cell offers a way to use solar power to efficiently split water into hydrogen and oxygen. A semiconductor electrode is used to generate electrical power from sunlight and drive the hydrogen and oxygen evolution reactions in aqueous environment. The work in this thesis aims to improve the understanding of the dynamics of the semiconductor electrode in a photoelectrochemical cell by implementing a numerical model of the system. The model is used to solve the carrier densities during the operation, when the charge carriers in the semiconductor are not in thermal equilibrium due to the incident radiation generating electron–hole pairs. The simulated results are compared to experimental study of different GaAs–based photoelectrodes.

For the experimental study both p– and n–type GaAs photoelectrodes were fabricated. In addition, a sample with a thin epitaxial n–type layer on a p–type substrate was studied. Chopped light voltammetry and electrochemical impedance spectroscopy measurements were used to characterize the samples. The results show that p–type GaAs is not effective as a photoelectrode due to large overpotential required before any photocurrent was observed. The n–type layer was found to slightly improve the results. The current from the n–type sample was observed to be significantly better, but this is likely to be attributed to dissolving of the sample instead of water splitting reaction. The implementation of the numerical model was successful, but the accuracy of the simulated results leaves room for improvement. The implementation of drift–diffusion model used for the simulation cannot explain all of the measured results, and a more sophisticated model would be required for predictive simulations. Based on the results, key issues are identified and future development ideas suggested.

Keywords: renewable energy, photoelectrochemical cell, water splitting, numerical simulation

AALTO-YLIOPISTO
SÄHKÖTEKNIIKAN KORKEAKOULU

DIPLOMITYÖN
TIIVISTELMÄ

Tekijä: Lassi Hällström

Työn nimi: GaAs–pohjaisten valosähkökemiallisten kennojen simuloinnit ja mittaukset

Päivämäärä: 22.01.2018 Kieli: Englanti Sivumäärä: 7+51

Elektroniikan ja nanotekniikan laitos

Professuuri: S–129 Sähköfysiikka

Työn valvoja: Prof. Ilkka Tittonen

Työn ohjaaja: M.Sc. Camilla Tossi

Valosähkökemiallinen kenno tarjoaa keinon käyttää aurinkoenergiaa tehokkaasti hajottamaan vettä vedyksi ja hapeksi. Puolijohde–elektrodi generoi sähkövirtaa auringon valon avulla sekä ajaa vedyn ja hapen kehitysreaktioita vesipitoisessa ympäristössä. Tämän diplomityön tavoitteena on tutkia puolijohde–elektrodin dynamiikkaa valosähkökemiallisessa kennossa kehittämällä numeerinen malli. Mallin avulla voidaan laskea varauskuljettajien tiheydet kennon toiminnan aikana, jolloin elektronit ja aukot eivät ole termisessä tasapainotilassa valaistuksen luomien varauskuljettajaparien vuoksi. Simuloituja tuloksita verrataan kokeelliseen työhön, jossa käytettiin erilaisia GaAs–pohjaisia elektrodeja.
Kokeellista työtä varten valmistettiin sekä p– että n–tyypin GaAs–elektrodit. Lisäksi valmistettiin p–tyypin näyte, jonka päälle kasvatettiin ohut n–tyypin kerros. Näytteistä mitattiin virta–jännite -käyrä katkotulla valaistuksella sekä sähkökemiallinen impedanssispektri. Tulokset osoittavat, että p–tyypin GaAs ei ole tehokas elektrodi veden hajottamiseen, sillä se vaatii korkean ylijännitteen ennen kuin valon tuottama virta on havaittavissa. Kasvatetun n–tyypin kerroksen havaittiin parantavan tuloksia. N–tyypin näytteen tuottama virta havaittiin huomattavasti paremmaksi, mutta todennäköisesti kyse on näyteen hajoamisreaktiosta veden hajottamisen sijaan. Tulosten perusteella numeerisen mallin tarkkuuden parantamiseksi esitetään jatkotoimia, sillä simulaation taustalla oleva fysikaalinen malli ei kykene selittämään aivan kaikkia mitattuja tuloksia.

Avainsanat: uusiutuvat energianlähteet, valosähkökemiallinen kenno, veden hajottaminen, numeerinen simulointi

Preface

I want to thank my supervisor Ilkka Tittonen and my instructor Camilla Tossi for their distinguished and incontrovertible guidance. May there be eternal glory to all other members of the MQS group for providing an inspiring atmosphere to work in. Thanks to all my friends within the academic community for supporting me throughout my studies, and to those outside it for keeping me reminded that science is not all that matters in life. Last, I want to thank my family for the same unconditional encouragement for my work towards this thesis that I have learned to expect from them.
Additionally, the financial support from the dean for purchasing the needed measurement equipment is acknowledged.

Otaniemi, January 2018

Lassi J. Hällström

Contents

Symbols and abbreviations

Symbols

A	area
c	speed of light in vacuum
C	capacitance
$C_{\mathcal{E}}$	scaling constant for electric field
C_j	scaling constant for carrier fluxes
C_p	scaling constant for carrier densities
C_x	scaling constant for position
C_ϕ	scaling constant for electrostatic potential
D	diffusion constant
e	Euler's number
E	energy
E_{red}	reduction potential
E^0	standard potential
E_g	band gap energy
E_F	Fermi level
$\mathcal{E}$	electric field magnitude
f	frequency
F	Faraday constant
G	Gibbs free energy
$G(x)$	carrier photogeneration rate
h	Planck constant
I	current
j_0	exchange current density
J	current density
k_B	Boltzmann constant
k_{tr}	transfer rate constant
n	electron density
n_i	intrinsic carrier density
n_{0i}	bulk equilibrium density of electrons
N_A	acceptor density
N_D	donor density
N_C	conduction band density of states
N_V	valence band density of states
p	hole density
p_{0i}	bulk equilibrium density of holes
P_s	solar power density
q	elementary charge
Q_r	reaction quotient
r_d	residual of differential equations
r_b	residual of boundary conditions
r_s	surface recombination rate
R	resistance, gas constant
$R(x)$	carrier recombination rate
$S(x)$	function for evaluating attempted solution

T	absolute temperature
U_c	chemical potential
U_e	electrochemical potential
V	voltage
V_H	Helmholtz voltage
V_{SC}	electrostatic voltage across semiconductor
V_{fb}	flat band voltage
V_{ref}	measured voltage against RHE
V_{th}	thermal voltage $V_{th} = k_B T/q$
w	depletion region width
x	position
X	solution mesh
Y	attempted solution
Z	impedance
α	absorption coefficient
ε	permittivity, $\varepsilon = \varepsilon_r \varepsilon_0$
χ	electron affinity
η	overpotential
η_{elec}	faradaic efficiency
η_{STH}	solar-to-hydrogen efficiency
κ	fitted component values
λ	wavelength
μ	mobility
τ	carrier lifetime
ϕ	electrostatic potential
Φ	photon flux, global error function
θ	phase angle
ζ	Fermi level distance from conduction/valence band

Abbreviations

ALD	atomic layer deposition
BVP	boundary value problem
DIW	de–ionized water
EIS	electrochemical impedance spectroscopy
IPA	isopropanol (isopropyl alcohol)
MOVPE	metalorganic vapor phase deposition
MQS	micro– and quantum systems
NHE	normal hydrogen electrode
RHE	reversible hydrogen electrode
SHE	standard hydrogen electrode
SEI	semiconductor electrolyte interface
PEC	photoelectrochemical

1 Introduction

Liquid hydrocarbon fuels have proved to be an irreplacable energy source for transportation. Quite recently electric vehicles have entered the market, but they suffer from high charging times, and low range and high cost compared to gasoline engine. The energy density of current battery technologies, both per volume and per mass, also prevents their use in aviation. The incentive to replace fossil fuels is not limited to mitigating climate change, but also includes concerns for fuel supply security. In order to pursue these goals, fossil fuel use should be reduced, but without a good alternative this would result in large socioeconomic issues. In addition to alternative technologies such as electric power, fossil fuels could also be replaced by synthetic, carbon neutral fuels. This solution would retain all the benefits of liquid hydrocarbon fuels such as high energy density and ease of transport, and could use the infrastructure already in place for distributing the fuel. Fuels produced from biomass, such as different plants or algae are already available. The work in this thesis is part of a research towards a completely synthetic hydrocarbon fuel, produced from water, and CO_2 captured from air using solar power.

Using electrolysis, water can be split into hydrogen and oxygen by applying electrical power. Depending on the source of the electrical power, this process can be used for environmentally friendly hydrogen production. By the end of 2017, majority of hydrogen production is done by extracting it from fossil hydrocarbons [1]. This method is counterproductive to the goal of replacing fossil fuels, and an efficient way of utilizing solar power to harvest hydrogen from water would be invaluable for moving towards carbon–neutral energy economy. Even with the rapid decline of the price of solar power, using traditional solar cells for driving water electrolysis remains inefficient [2, 3]. An alternative solution for a water splitting system is to use a photoelectrochemical (PEC) cell, where a semiconductor photoelectrode acts simultaneously as the solar absorber and reaction–driving electrode. The PEC cell as a technology offers potential for higher efficiencies than photovoltaic electrolysis due to the direct coupling of the photon absorption and electrolysis [4]. It also offers economical advantages due to its simpler design and reduced fabrication cost.

The first PEC cell was presented already in 1972 [5]. By the end of 2017, there has been a lot of research arising in the field of PEC cells, but no commercial applications exist. Although PEC cells offer an evironmentally friendly way to store solar energy with good scaling potential [6], in order to economically compete with fossil fuels, the total efficiency of the system has to be increased [3]. A state of the art multijunction PEC cell can reach solar-to hydrogen efficiency of 16% [7]. Regardless of the extensive research on the topic, the dynamics of a PEC system are not well understood, and time consuming experimental studies are required to quantify the effects of design choices. [8, 9] The number of parameters affecting the efficiency is not limited to the material choice, but also includes the electrolyte solution and advanced techniques such as deposition of co-catalyst nanoparticles on the semiconductor surface. [10–13]

The work in this thesis aims toward a numerical model that could predict the effect of different system parameters on the efficiency of the cell. A reliable model would enable research on PEC cells by educated design, as opposed to screening the effects

of different parameters via experimental study.
In this thesis, a numerical model for a semiconductor photoelectrode in a photoelectrochemical cell is implemented. Section 2 will explain the relevant theoretical background and those physical phenomena on which the model is based. A detailed explanation of the mathematics used for solving the numerical system is provided in section 3. For the experimental study, the sample fabrication and methodology for the electrochemical measurements are presented in section 4, and all the results for both the simulation and experimental parts in section 5. Finally, in Section 6 a conclusion is provided and some insight to the future of the research of this thesis is offered.

2 Theory of photoelectrochemical cells

This section will offer an overview of the theoretical background of photoelectrochemical cells with the focus on the phenomena that are most relevant to this work. Multidisciplinary research often runs into inconsistent terminology, and the topic of photoelectrochemical water splitting is not an exception. Therefore, the relevant terminology, as it is used in this thesis, is defined so that the connection between the concepts in chemistry and semiconductor physics is clear.

2.1 The reference potential

The cell potentials in any electrochemical cell are typically defined as standard potentials, which are potentials measured against a hydrogen electrode that has a defined standard electrode potential of 0 V at specific conditions. There are two conventions for these conditions: the normal hydrogen electrode (NHE)[10, 12, 14–17] and the standard hydrogen electrode (SHE)[18–20]. For most purposes the SHE and the NHE can be considered identical, but there is a difference in their definitions[21]. Both are defined as the potential of the reaction shown in eq. (2.1) on a platinum electrode acting as a catalyst at 25 °C. The platinum itself takes no part in the reaction.

$$2\,H^+ + 2\,e^- \longrightarrow H_2. \tag{2.1}$$

The NHE is defined in a 1 N (normality) acid with hydrogen bubbled through it at 1 atm pressure (101 325 Pa) [21]. This system can be realized, but the exact measured potential depends on activity and fugacity instead of concentration and gas pressure. Chemical activity is the effective concentration of a species, and will differ from the concentration in any non–ideal solution. Fugacity has a similar relation to partial pressure as the activity has to concentration: it is the effective partial pressure that takes into account the non–ideal behaviour of any real gas. The SHE is then defined in a solution of 1 M (molarity) of H^+ with activity of unity and H_2 fugacity of 100 kPa [22]. This definition is exact, but it ignores the effects of the ionic interaction between the H^+ ions and treats hydrogen as ideal gas. Therefore this is a theoretical ideal solution that cannot be constructed in reality.[21, 23] The difference of potential between the NHE and the SHE is only 5.7 mV, assuming hydrogen ion activity of 0.8 for the NHE.[21] In many recent publications NHE and SHE are used interchangeably, or even claimed to be the equivalent to each other[23–25], so it can be argued that the definition of the NHE has changed to be equal to SHE. The standard electrode potentials for all real electrodes are defined as the difference in their reaction potential versus the SHE. For all measurements in this thesis a third standard, the reversible hydrogen electrode (RHE), is used instead. The RHE is defined as the potential of the same reaction used for SHE and NHE, eq. (2.1). However, as it is used in various solutions of different pH values, its standard potential changes according to the Nernst equation shown in eq. (2.2). The RHE is a realizable version of the SHE, that can be used directly in the solution of

the experiment, and it has lately become a popular choice as a reference electrode [6, 26].[20]

The Nernst equation for a half–cell reduction potential is

$$E_{red} = E^0_{red} - \frac{RT}{zF} \ln Q_r, \tag{2.2}$$

where E_{red} is the reduction potential at conditions defined by Q, E^0_{red} the standard reduction potential, R the gas constant, T the absolute temperature, F the Faraday constant, z the number of electrons transferred in the half–cell reaction and Q the reaction quotient describing the ratio of the activities of the different reactants. For the hydrogen electrode reaction given in eq. (2.1), eq. (2.2) simplifies to

$$E^0_{RHE} = E^0_{SHE} - 0.059[V]\text{pH}. \tag{2.3}$$

The constant $0.059\,\text{V} \approx 2.3qk_BT$ is a product of an approximation of the conversion from natural to base 10 logarithm used in the definition of the pH value and the thermal voltage $V_{th} = qk_BT$ at 25 °C.

In short, the chemical potential scale is defined by $E^0_{SHE} = 0\,\text{V}$, and measurements can be related to the scale by measuring potentials against RHE and then using eq. (2.3). In solid state physics, the energy levels inside a semiconductor are related to the local vacuum level via the electron affinity. The electron affinity is the energy needed to move an electron from vacuum immediately outside the semiconductor into the conduction band. The potential against the local vacuum level At standard conditions of 25 °C temperature and 1 bar pressure the absolute potential of the SHE is by defined as approximately $-4.44\,\text{V}$. [27], so it follows that the absolute potential of the RHE varies with the pH of the electrolyte. At pH 0 $E^0_{RHE} = E^0_{SHE} = 0$.

2.2 Electrochemical and electrostatic potential

Electrochemical potential refers to the voltage that can be measured across the device, which is the difference of the Fermi levels between the measurement points. When the system is in thermal equilibrium, there is no net current and therefore no electrochemical potential difference. Any initial differences in the Fermi levels will be neutralized by charge accumulation, which will generate electric fields in the system. In equilibrium the drift current related to the field is counteracted by diffusion of the charge carriers towards lower concentration, resulting in zero net current. The electric potential, or electrostatic potential of a charge is defined as the amount of work done against an electric field in order to move the charge, in this case an electron.

$$\phi(x) = -\int_{x_0}^{x} \mathcal{E}(x)dx, \tag{2.4}$$

where ϕ is the electrostatic potential, x the spatial coordinate, x_0 a reference point of zero potential and $\mathcal{E}$ the electric field. Just like the drift and diffusion currents, the

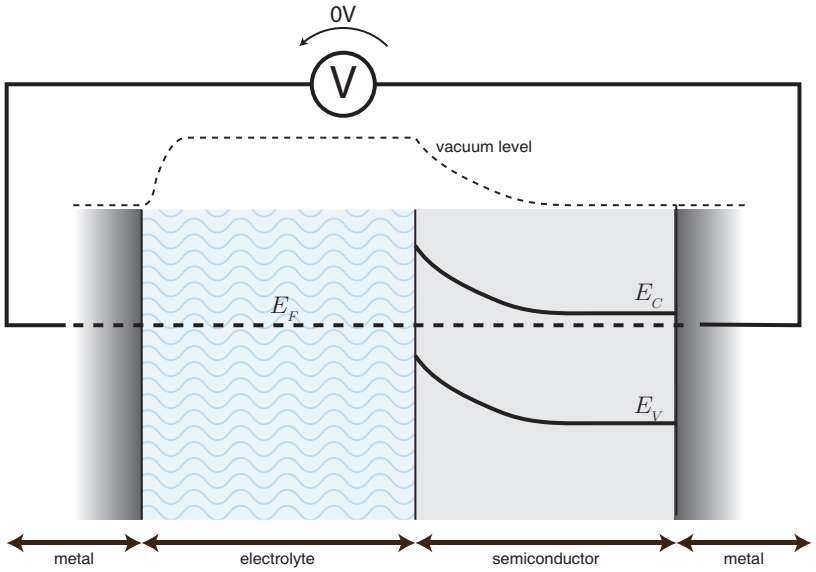

Figure 1: A simplified band diagram of a PEC cell. The vacuum level follows the electrostatic potential curve caused by the charge accumulation at the interfaces. However, the electrochemical potential, or the Fermi level E_F, is constant across the whole system, and the external voltage measured by a voltmeter is zero. There is no net carrier flow i.e. electric current anywhere in the system.

gradients of the electrostatic potential are cancelled by the corresponding gradient in the chemical potential of the electrons, which is caused by the uneven concentration of the carriers. The total effective, measurable potential in the system is the electrochemical potential of the electrons, which is the sum of the electrostatic potential resulting from the charge distribution and the chemical potential resulting from the concentration distribution.

$$U_e(x) = \phi(x) + U_c(x), \tag{2.5}$$

where U_e is the electrochemical potential and U_c the chemical potential. This total electrochemical potential is more rigorously defined as the partial derivative of a free energy in a system with respect to the amount of species in the system. Assuming that temperature and pressure are held constant,

$$U_e(x) = \frac{\partial G}{\partial N}, \tag{2.6}$$

where G is the Gibbs free energy and N the number of electrons in the system. This can be interpreted as the average amount of work required to add an electron to the system, and it follows that the electrochemical potential is equal to the Fermi level. Even though the electrostatic potential has no direct influence over the effective voltage or current of the system, it is still an important quantity when analyzing a semiconductor system. The conduction and valence band positions as well as the local vacuum potential depend on the electrostatic potential, and therefore are not necessarily constant when the system is in equilibrium. The vacuum level bending has to be accounted for when the vacuum level is used as a reference. This is also

why any reference has to be at the local vacuum level at a specific point, as the vacuum level will not be constant over the whole system. Figure 1 shows an example of a semiconductor photoelectrochemical cell with a flat Fermi level and resulting bending of the conduction and valence bands and the vacuum level. In the electrolyte region, the local vacuum level is by definition 4.44 V above the SHE, so that the absolute potential at the local vacuum level of the electrolyte is 0 V.
As voltage is defined as the difference in potential, it is necessary to state which definition of potential is used when discussing voltage. In this thesis, voltage refers to the difference of the electrochemical potential, unless explicitly stated otherwise.

2.3 The Fermi level

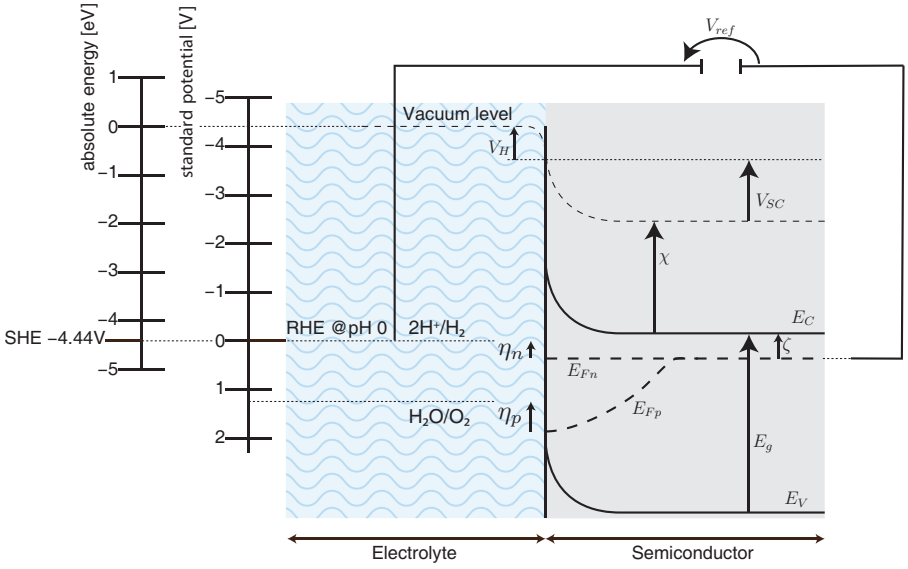

Figure 2: Potential diagram of a N–type cell under illumination. The absolute energy and standard potential are connected by the absolute potential of the SHE at −4.44 V. The voltage between the reference electrode and the Fermi level at the rear surface of the semiconductor V_{ref} can be measured. The electron affinity χ, the Fermi level distance from the conduction band in the bulk ζ, and the band gap energy E_g are known properties of the semiconductor. V_H is the Helmholtz voltage and V_{SC} the electrostatic potential drop across the semiconductor.

The standard potential of a semiconductor electrode is defined by its Fermi level position at the electrolyte interface. The conduction band position is related to the local vacuum level via the work function of the semiconductor, but finding the Fermi level position is a little more complicated. The Fermi level in a semiconductor can be thought of as an energy level at which there is a 50% chance that an energy state is occupied by an electron. The probability of an energy state being occupied at thermal equilibrium is given by the Fermi-Dirac distribution

$$f(E) = \frac{1}{1 + e^{\frac{E - E_f}{k_B T}}}, \tag{2.7}$$

where E_f is the Fermi level, so that $f(E_f) = 0.5$. Assuming that the exponential term in eq. (2.7) is large enough the distribution can be approximated with the Maxwell-Boltzmann distribution

$$f(E) \approx e^{-\frac{(E-E_F)}{k_B T}}. \tag{2.8}$$

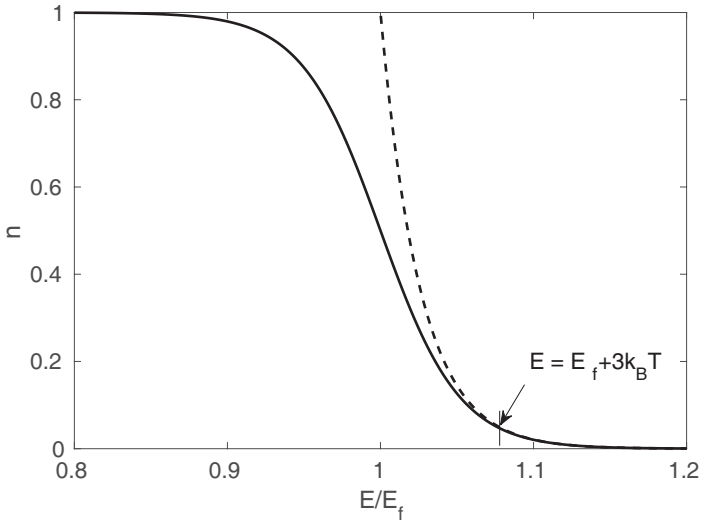

Figure 3: Comparison of the Fermi-Dirac distribution (solid line) and Maxwell-Boltzmann distribution (dashed line). The x-axis shows the energy relative to the Fermi level and the y-axis the fraction of the filled states. The conventional limit of a good approximation, $E = E_f + 3k_BT$ is marked.

Conventionally used limit for the approximation is $|E - E_f| \geq 3k_BT$, which results in the exponential term having a value of $e^3 \approx 20$ and an error of under 5% in the probability distribution. This is illustrated in fig. 3. The Maxwell–Boltzmann approximation is practical, because it allows relating the carrier densities to the Fermi level position analytically. The derivation of these relations is not included here, but the resulting equations are: [28]

$$n = N_C e^{\frac{E_F - E_C}{k_B T}} \tag{2.9a}$$

$$p = N_V e^{\frac{E_V - E_F}{k_B T}}, \tag{2.9b}$$

where N_C and N_V are the effective densities of states in the conduction and valence bands. In thermal equilibrium the carrier densities are related to each other via

$$np = n_i^2, \quad n_i = \sqrt{N_C N_V} e^{-\frac{E_g}{2k_B T}}, \tag{2.10}$$

where n_i is the intrinsic carrier density. Assuming full ionization of the dopant atoms the majority carrier density is equal to the doping density of the semiconductor, and the minority carrier density is found with eq. (2.10). The result is that the Fermi

level position relative to the conduction and valence bands depends on the doping of the semiconductor: in n–type materials it is located near the conduction band and in p–type materials near the valence band.
As mentioned earlier, the Fermi level in a material is equal to the local electrochemical potential of electrons. A direct consequence is that the electrochemical potential, or Fermi level, of electrons is constant in thermal equilibrium state. It also follows that the measurable voltage from the back surface of the semiconductor to the electrolyte is the voltage between the Fermi level in the semiconductor and the RHE. In order to make any use of this measured voltage, a way to connect the Fermi level to the electrochemical scale is required. This is where the vacuum level becomes useful, as the conduction band position of a semiconductor is directly related to the vacuum level via the electron affinity. The separation between the Fermi level and the conduction band at the back surface can be solved from (2.9). Assuming an ohmic contact at the back surface the majority carrier density will always be close to equilibrium value, and equal to the doping density. For n–type semiconductor

$$\zeta = E_F - E_C = \ln \frac{N_C}{N_D}, \tag{2.11}$$

where ζ is the fermi level distance from the conduction band and N_D the donor density. The distance of the Fermi level from the valence band can be calculated in similar fashion for p–type materials.

The two remaining unknown elements of the energy diagram in fig. 2 are the Helmholtz voltage V_H and the electrostatic potential drop across the semiconductor V_{SC}. Knowledge of the electrostatic potential drop across the semiconductor is essential for the implementation of the numerical simulation. Relating V_{SC} to the measured voltage V_{ref} is straightforward after the Helmholtz voltage is known. Methods for estimating the Helmholtz voltage will be discussed in section 2.6.

When the semiconductor piece is taken out of thermal equilibrium, for example by illumination with sufficiently energetic photons, eq. (2.10) no longer holds and the Fermi levels defined in eqs. (2.9) are not equal to each other. However, the relations in eqs. (2.12) can still be used by simply treating these separate Fermi levels for electrons and holes as quasi–Fermi levels. [28]

$$n = N_C e^{\frac{E_{Fn} - E_C}{k_B T}} \tag{2.12a}$$

$$p = N_V e^{\frac{E_V - E_{Fp}}{k_B T}}. \tag{2.12b}$$

Even if the system is not in thermal equilibrium, it can still reach a state where the photon and carrier fluxes in and out of the system are constant and the system itself is in a steady, quasi–static state. This quasi–equilibrium model is valid when the carrier scattering time constant is smaller than the smallest time constant of the device, such as the modulation frequency of the illumination. In general, in order for a dynamic system to reach a steady state, the system response has to be faster than the changes in the input. For electrochemical measurements this is not an issue, since typical scattering times for semiconductors are on the order of 100 fs [28], while the

fastest timescale of interest is up to 1 MHz impedance spectroscopy measurement, which corresponds to 1 µs.

2.4 Electrochemical reactions

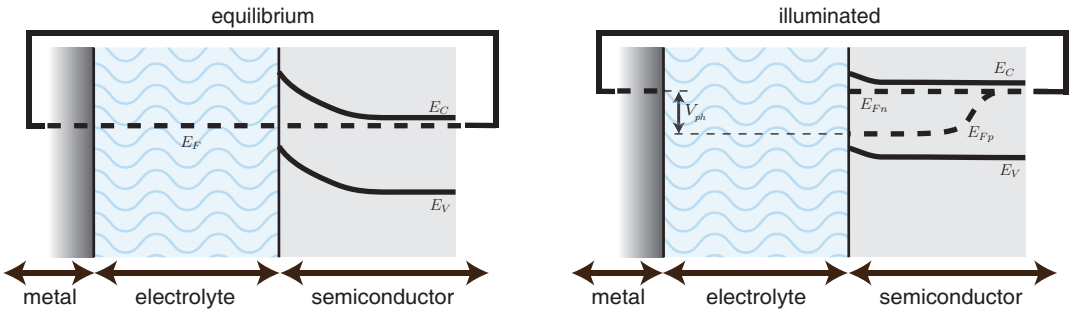

Figure 4: Minimal example of photoelectrochemical cell with n-type semiconductor. When the semiconductor and the metal counter electrode are short circuited, the electron quasi-Fermi level aligns with the Fermi level of the metal. In dark equilibrium these Fermi levels set to the level of the electrolyte redox potential, forming a single flat Fermi level across the whole device. When illuminated, the Fermi level in the semiconductor is split into quasi–Fermi levels, generating photovoltage and photocurrent.

Simply put, a photoelectrochemical cell is a device that acts simultaneously as a photoelectric cell generating electricity from sunlight and an electrochemical cell driving an electrochemical redox reaction. A minimal example of this is a semiconductor working electrode and a metal counter electrode immersed in electrolyte solution and connected by a wire, shown in fig. 4. The semiconductor working electrode is responsible for the photoelectric part of the cell that creates the photovoltage responsible for driving the cell current. Absorbed incident light generates free electron–hole pairs that are then separated by the electric field that is present at the semiconductor–electrolyte interface (SEI). In a cell made of n–type semiconductor the holes are the minority carriers and they also flow towards the electrolyte interface where they reduce oxygen from water. The electrons flow to the back surface of the semiconductor and then via the wire to the counter electrode. Assuming that the carriers have sufficient electrochemical potential to exceed the water stability region shown in fig. 5, the excess electrons and holes then react with the electrolyte according to the reactions shown in eqs. (2.13) to (2.16):[5][25]

$$4\,\mathrm{OH^-} + 4\,\mathrm{h^+} \longrightarrow 2\,\mathrm{H_2O} + \mathrm{O_2} \qquad E^0_{ox} = 0.401\,\mathrm{V}, \tag{2.13}$$

$$4\,\mathrm{H_2O} + 4\,\mathrm{e^-} \longrightarrow 2\,\mathrm{H_2} + 4\,\mathrm{OH^-} \qquad E^0_{red} = -0.829\,\mathrm{V}, \tag{2.14}$$

where h^+ is an electron hole in the valence band of the semiconductor. With acidic electrolyte the reactions are:

$$4\mathrm{h^+} + 2\,\mathrm{H_2O} \longrightarrow \mathrm{O_2} + 4\,\mathrm{H^+} \qquad E^0_{ox} = 1.229\,\mathrm{V}, \tag{2.15}$$

$$4\mathrm{e^-} + 4\,\mathrm{H^+} \longrightarrow 2\,\mathrm{H_2} \qquad E^0_{red} = 0\,\mathrm{V}. \tag{2.16}$$

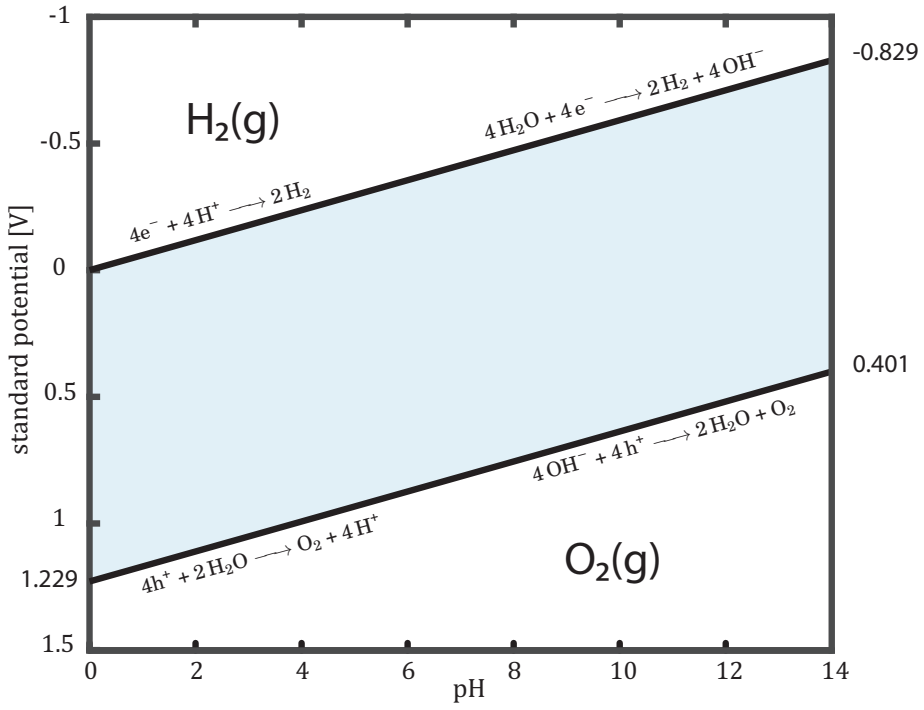

Figure 5: Pourbaix diagram of water showing the stable region of water. The shaded area marks the region where water is stable. At lower potentials hydrogen gas is formed and at higher potentials oxygen. At low pH values the active ion in the solution if H^+ and respectively at high pH the reactions involve OH^-

With an n-type cell the oxidation reaction happens at the semiconductor electrode (anode) and the reduction at the counter electrode (cathode). A p–type semiconductor acts as the cathode driving the hydrogen evolution instead. The total reaction is in both cases

$$2\,H_2O \longrightarrow O_2 + 2\,H_2. \tag{2.17}$$

The standard reaction potential values E^0 are all given as reduction potentials, but eqs. (2.13) and (2.15) are in this case oxidation reactions. The total cell potential is then given by

$$E^0_{cell} = E^0_{red} - E^0_{ox}. \tag{2.18}$$

The oxidation reactions are usually written with electrons e^- on the right hand side instead of holes h^+ on the left hand side. In this thesis the hole notation is used as the hole flow dynamics ties the reactions more intuitively to the semiconductor physics and to the simulation results.

Even though adjusting the pH value has no effect on the total reaction potential, increasing the concentration of the ions taking part in the reaction results in faster kinetics and reduces the effect of the electrolyte on the measurements. Splitting

Table 2: Effect of the doping type of the semiconductor electrode

N type	P type
photoanode	photocathode
holes react	electrons react
oxidation	reduction
oxygen evolution	hydrogen evolution
$4\,h^+ + 2\,H_2O \longrightarrow O_2 + 4\,H^+$	$4e^- + 4\,H^+ \longrightarrow 2\,H_2$

of pure water is also made difficult by the low conductivity, and either strong acid or strong base is typically used [29]. The mathematical model implemented in this thesis also assumes high enough ion concentration in the electrolyte so that the current is limited only by the properties of the semiconductor. Regardless of the pH of the electrolyte the total potential of the water splitting cell is $-1.23\,V$ at standard conditions, which corresponds to energy of $236.96\,kJ/mol$. This is the minimum voltage required to drive the reactions and as such gives a lower bound for the semiconductor band gap in water splitting cells. In practice a non-zero overpotential is needed in addition to the $1.23\,V$ to have a driving force for overcoming the kinetic barriers of the reaction. In other words, the reaction can thermodynamically happen at $1.23\,V$ but it would be infinitely slow. Additionally, the energy released by hydrogen combustion is $285.58\,kJ/mol$, which is higher than the minimum electrical energy input. The energy difference is provided by the reaction consuming heat from the environment in addition to electricity. In order to drive the reaction isothermally, a voltage of $1.481\,V$ is required. [30]. In practice this makes little difference, as part of the incident radiation is absorbed into heat anyway. A commonly used kinetic model for metal electrodes is the Butler-Volmer equation, shown in eq. (2.19). The total current is the sum of anodic and cathodic currents represented by the exponential terms and approaches zero with zero overpotential.

$$j = j_0 \left(e^{\frac{\alpha_a z F \eta}{RT}} - e^{-\frac{\alpha_c z F \eta}{RT}} \right), \tag{2.19}$$

where η is the overpotential, i.e. potential exceeding the redox potential of the reaction that is driven at the electrode, α is the charge transfer coefficient j is the actual current density, j_0 is the exchange current density and z is the number of electrons transferred in one reaction. A similar relation exists for semiconductor electrodes, called the Gerischer model, that accounts for the energy difference between the conduction and valence bands [25]

$$j_p = j_0^p e^{\frac{\eta_p}{V_{th}} - 1} \tag{2.20}$$

$$j_n = j_0^n e^{\frac{-\eta_n}{V_{th}} - 1}, \tag{2.21}$$

where j_0^p and j_0^n are the exchange current densities for holes and electrons, and j_p and j_n the actual hole and electron currents. This model was used as the boundary condition at the SEI for the numerical model implementation.

2.5 Fermi level of the electrolyte

The Fermi level of the electrolyte, also called redox potential, is somewhat ambiguous term, as there are no free electrons in the solution. The electrons in the ions do however have electrochemical potential, and the Fermi level of the electrolyte can then be defined as the average potential of these electrons. In a thermal equilibrium the Fermi levels of any electrodes in the electrolyte will align with the Fermi level of the electrolyte, assuming that the transient charge transfer before the system achieves the equilibrium state does not significantly affect the Fermi level of the electrolyte. As the volume of the electrolyte is typically orders of magnitude larger than the space–charge region formed in the semiconductor, this assumption can be considered valid. The exact value of the redox potential depends on the pH of the solution according to the Nernst equation, meaning it has the same 59 mV/pH slope as the hydrogen and oxygen evolution reactions. The location of the redox potential between the water stability limits then depends on the relative activity of the H_2 / H_2O and H_2O / O_2 redox couples [25]. The reaction activities depend not only on the concentration of the respective ions (pH), but also on the concentration of dissolved O_2 and H_2, with high O_2 concentration bringing the redox potential closer to the oxygen evolution potential.[30]. As all electrolytes used in the measurements for this thesis were purged of dissolved oxygen with nitrogen, the electrolyte Fermi level is assumed to lie close to the hydrogen evolution potential, which is approximately 0 V vs. the RHE at any pH.

2.6 Helmholtz layer

The name 'Helmholtz layer' is commonly used to refer to any double layer model that forms in a liquid in contact with a solid surface. The dynamics of the layer formation depend heavily on the properties of both the solid surface and the liquid. The simplest model for the Helmholtz layer is that the ions in the electrolyte will form a charged layer as a reaction to the electric field created by the space–charge region in the semiconductor electrode. In the case of this thesis the surface material for the samples is TiO_2, which is in itself an ionic oxide material and will have oxygen vacancies at the surface that adsorb hydroxyl groups (OH^-) from the electrolyte. These groups will then reach an equilibrium with the electrolyte that depends only on the pH of the electrolyte and not on the charge in the semiconductor side of the interface. This kind of surface is better modeled with a Stern model, that includes separate adsorption and diffuse surface layers as shown in fig. 6. At the electrolyte side of the SEI, the ions in the solution will adsorb on the electrode surface forming a charged layer. This is the inner layer of the Stern model, and its composition is determined mostly by the available ion concentrations, which are related to the pH value of the electrolyte. Just outside the adsorption layer layer is the Gouy–Chapman region, which is the diffuse charge layer created by the electric field of the space–charge region of the semiconductor.[31]
The potential drop across the inner layer can be modeled as a simple equilibrium of

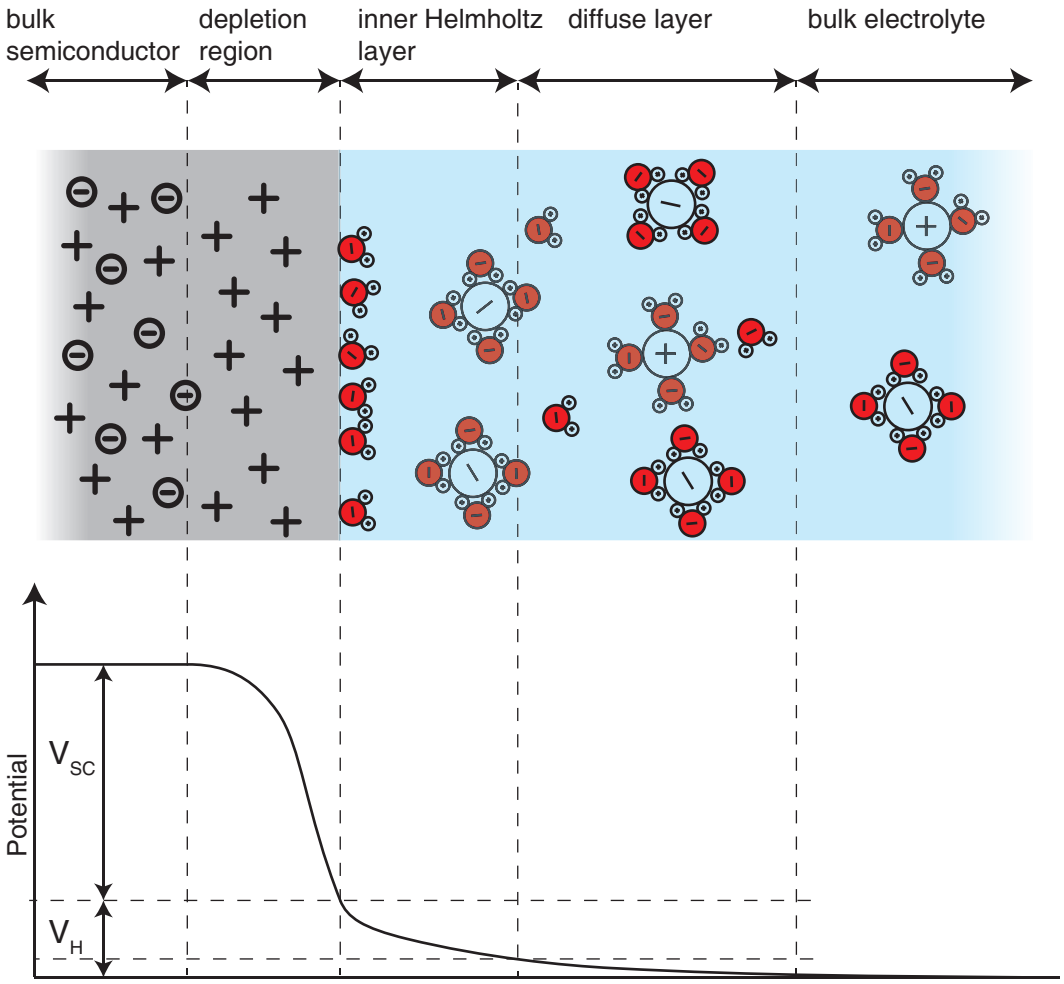

Figure 6: The formation of the electrical double layer at the SEI. Depending on the operating point of the electrode, a depletion region forms inside the semiconductor. This attracts opposite charge from the electrolyte, forming a charged layer on the electrolyte side. Beyond the Helmholtz layer a diffuse layer is formed, where the ion concentration reaches the bulk value. In this thesis the potential drop across the diffuse layer is included in V_H.

adsorbed ions on the surface,

$$\frac{[\mathrm{H_S}^+]}{[\mathrm{H_3O}^+]} = a e^{\frac{V_H}{V_{th}}}, \tag{2.22}$$

where $[\mathrm{H_S}^+]$ is the concentration of adsorbed hydrogen ions, $[\mathrm{H_3O}^+]$ the concentration of hydronium ions in the electrolyte and a some constant. Setting $V_H = 0$ at $\mathrm{pH} = \mathrm{pH_{IEP}}$ leads to

$$V_H = 2.3 V_{th}(\mathrm{pH} - \mathrm{pH_{IEP}}), \tag{2.23}$$

where $\mathrm{pH_{IEP}}$ is the isoelectric point, defined as the point of zero net surface charge. For TiO_2 $\mathrm{pH_{IEP}}$ is around 5.8–7.5. [31]. However, the validity of eq. (2.23) is not guaranteed for all materials, and also determining the value of $\mathrm{pH_{IEP}}$ experimentally would be difficult. Another approach is to find the flat band potential, and use it to calculate the potential drop across the Helmholtz layer.

2.7 The Flat band potential

The flat band potential is the measured potential V_{ref} required to eliminate the band bending caused by the alignment of the Fermi levels at equlibrium. At flat band conditions, there is no electrostatic potential drop across the semiconductor, and the only unknown quantity is the Helmholtz voltage.

$$V_H = E_{SHE}^{abs} - \frac{1}{q}(\chi + \zeta) + V_{fb}^{SHE}, \tag{2.24}$$

where $E_{SHE}^{abs} = -4.44\,\mathrm{V}$ is the absolute potential of the SHE and V_{fb}^{SHE} the measured flat band potential against the SHE. The flat band potential can be found by measuring the capacitance of the space–charge layer at the semiconductor side of the SEI as function of the measured voltage V_{ref}. Using the depletion region approximation for the semiconductor, the relation between the measured voltage and capacitance is given by the Mott–Schotky equation

$$\frac{1}{C^2} = \frac{2}{\varepsilon q N_D A^2}(V_{ref} - V_{fb} - V_{th}), \tag{2.25}$$

where C is the capacitance in the depletion region, ε the permittivity of the semiconductor, N_D the doping density, A the surface area and V_{fb} the flat band potential against RHE [25]. The inverse square of the measured capacitance should have a linear dependence on the measured voltage, and the flat band potential can be found by extrapolating the linear relation to $C^{-2} = 0$. When the capacitance–voltage relation is known, the doping density can be solved from eq. (2.25), resulting in

$$N_D = \frac{2}{\varepsilon q \frac{\Delta C^{-2}}{\Delta V_{ref}}}, \tag{2.26}$$

where $\frac{\Delta C^{-2}}{\Delta V_{ref}}$ is the slope of the linear relationship. For highly doped semiconductors the distance of the Fermi level from the conduction band at the back contact ζ is relatively small. The flat band potential relative to the hydrogen and oxygen reaction potentials can then be related to the band edge positions at the SEI, and therefore the ability of the semiconductor to drive the reactions. Additionally, the slope of the line gives information about the doping density of the semiconductor via

$$N_D = \frac{2}{(q\varepsilon \frac{\Delta C^{-2}}{\Delta V}}). \tag{2.27}$$

Equations (2.25) and (2.27) can be also used for p–type semiconductors simply by substituting $N_D = -N_A$. In other words, a negative slope of the measured inverse square of the capacitance against the voltage implies p–type doping.

2.8 Semiconductor physics

When a semiconductor material is hit by a photon, there is a chance that the photon gets absorbed. If the energy of the photon is sufficiently high, it can lift an electron from the valence band of the semiconductor to the conduction band and form what is called an electron-hole pair. The minimum energy needed for this to happen is the band gap energy of the semiconductor, which is a property of the specific material used. Any photoelectric system designed for energy production will eventually have to work efficiently using natural sunlight as the illumination source. The AM1.5G spectral irradiance, which is the solar irradiance when filtered with 1.5 times the average thickness of the Earth's atmosphere, is shown in fig. 7 [32]. However, as one photon will only ever be able to generate one electron–hole pair, a more relevant quantity is the photon flux of the sun. The spectral photon flux can be calculated from the spectral irradiance by

$$\Phi(\lambda) = \frac{E_e(\lambda)}{\frac{hc}{\lambda}}, \tag{2.28}$$

where Φ is the photon flux in photons per area per wavelength and E_e the spectral irradiance. This can be converted to a function of the photon energy by

$$\Phi(E_{ph}) = \frac{\Phi(\lambda)}{\frac{\partial E_{ph}}{\partial \lambda}}, \quad \frac{\partial E_{ph}}{\partial \lambda} = \frac{hc}{\lambda^2}, \tag{2.29}$$

where E_{ph} is the photon energy. This photon flux per unit area per photon energy is shown in fig. 8. The number of absorbed photons equals the number of generated carriers, which will directly affect the amount of generated photocurrent.

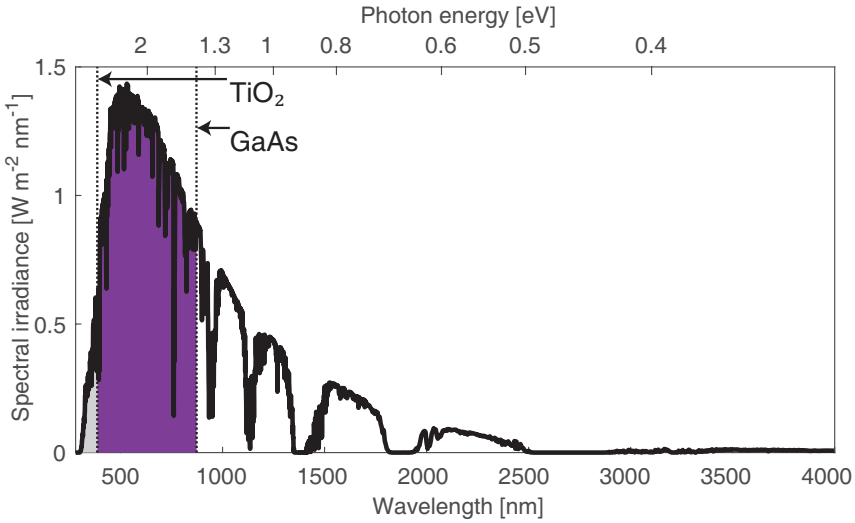

Figure 7: Spectral irradiance of AM1.5G solar radiation spectrum. Data from [32].

After the creation of the hole-electron pair, both charge carriers are affected by both diffusion due to the uneven concentration of the carriers and drift due to the

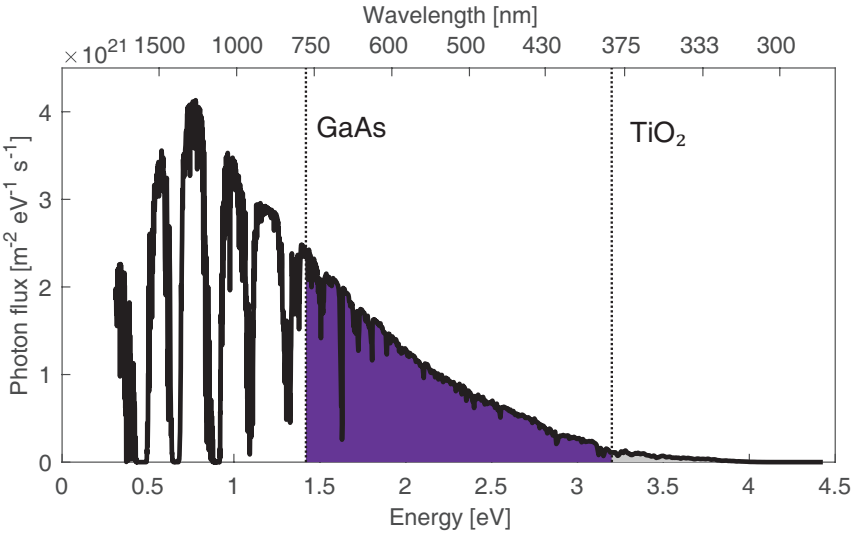

Figure 8: Spectrum from fig. 7 with photon flux as function of energy. The band gaps and usable part of the flux for GaAs ($E_g = 1.42\,\text{eV}$) and TiO_2 ($E_g = 3.2\,\text{eV}$) are marked.

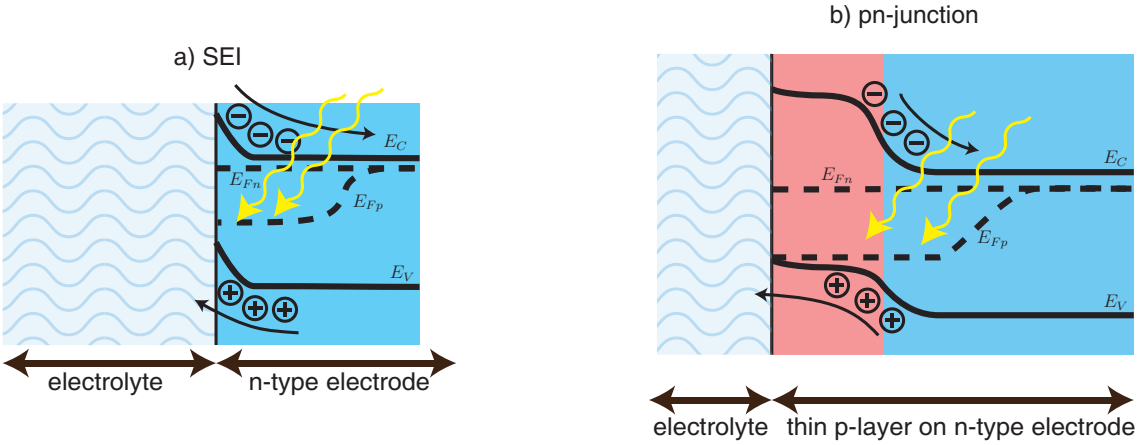

Figure 9: Two possible charge separation processes. a) at the SEI, b) at pn–junction.

electric field generated by the charge distribution. A space–charge region formed in a pn–junction or at the SEI will cause the opposite charges to separate. Both carriers are generated at the same rate, but the generation of the minority carriers has a much larger relative impact to the local carrier density and consequently the quasi–Fermi level. In the case of a buried junction as shown in fig. 9 b), the pn–junction will dominate the charge separation and the effective current direction. The carriers flowing to the electrolyte are now the majority carriers, and the larger available concentration of reactive carriers should increase the reaction rate[33, 34]. The excess carriers distributed throughout the semiconductor will tend to reach equilibrium via recombination. The recombination of the photogenerated carriers is lost in energy and with the help of the proper design of a photoelectric cell one should try to avoid this recombination loss. The mathematical representation of the charge separation and current flow in the cell is more thoroughly discussed in section 3.

Good light absorption properties are clearly required from the semiconductor in order to provide energy to drive the reaction. Semiconductor light absorption has been extensively studied for electricity production with solar cells, and the maximum efficiency for converting solar energy to electricity is with a band gap of 1.34 eV for a single pn junction, as shown in fig. 10 [35]. This is known as the Shockley-Queisser limit, named after the scientists who discovered it in 1961 [36]. Low band gaps will be able to absorb most of the solar photon flux, but most of the power from the photons is lost. Any single photon will only generate a single electron–hole pair, that is limited to the energy of the band gap. On the other hand, too high band gap will prevent large part of the spectrum from being absorbed at all.

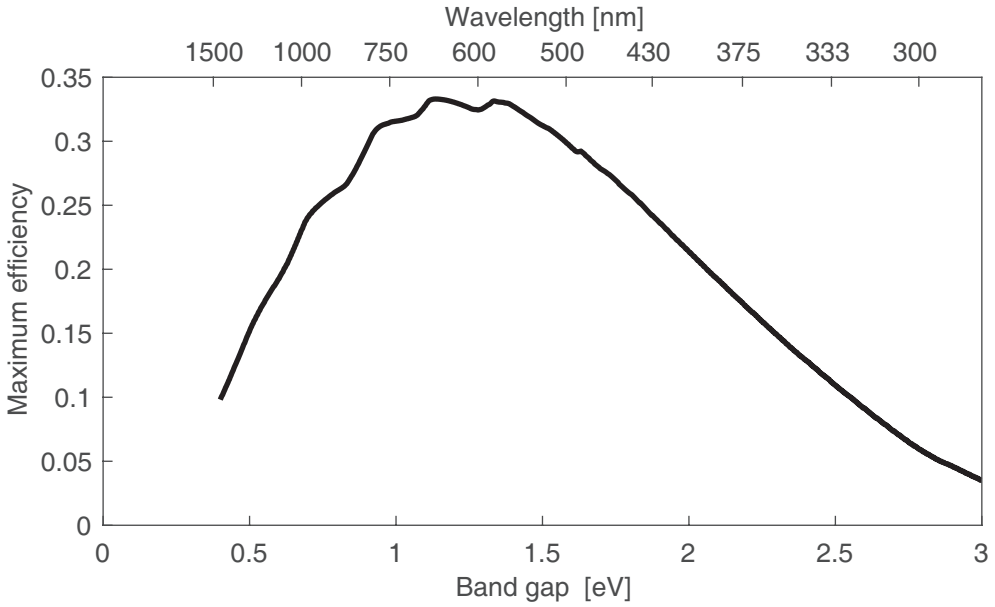

Figure 10: Schockley–Queisser maximum single junction solar cell efficiency.

2.9 The photoelectrochemical cell

Combining the theories of using semiconductors for photogeneration of light and chemical reactions for water splitting in aqueous electrolytes allows the use of sunlight to generate hydrogen and oxygen from water. The simplest way to achieve this goal is to connect traditional solar cells in series for large enough voltage and drive the electrolysis through metal electrodes. However, the solar–to–hydrogen efficiency of the complete system can be improved by using the semiconductor as an electrode directly in a PEC cell[4].

Many different materials have been considered for the semiconductor part of the photoelectrochemical cell. The requirements of a good material choice are quite strict, and there seems to be no consensus for an optimal material. The properties required from a good material for water splitting applications are [37]

- good light absorption

- band edges beyond the potential required to drive the reaction
- chemical stability
- efficient charge transport
- low overpotentials for the redox reaction(s)
- low cost

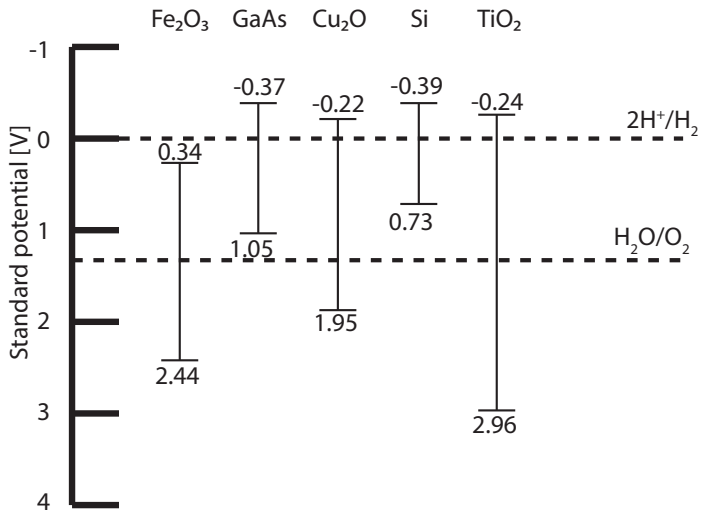

Figure 11: Energy band locations and band gaps of some semiconductors considered for photoelectrochemical cells at pH 0. The band edge positions in this figure are calculated directly from the electron affinity, and do not take into account the potential drop in the Helmholtz layer.

Figure 11 shows the band edge locations of some semiconductor materials that have been proposed for use in photoelectrochemical cells. These band edge positions do not account for any potential drop in the Helmholtz layer, and may vary drastically between applications. They are, however, a useful starting point when trying to figure out if a specific material could be used for water splitting.

The optimal absorption efficiency at $E_g = 1.34\,\mathrm{eV}$ is only barely above the $1.23\,\mathrm{V}$ that is required for the water splitting reactions, assuming that the band edges can be positioned perfectly to straddle the hydrogen and oxygen evolution reactions. Even with perfect band edge positioning, driving the reactions at any reasonable rate requires application of overpotential, typically at least $0.5\,\mathrm{V}$ [12, 26]. When this kinetic loss is combined with the thermodynamic losses of the system, and taking into account that the actually useful potential difference is not between the conduction and valence bands but between the quasi–Fermi levels [29], a realistic minimum band gap for a water splitting cell is approximately $2\,\mathrm{eV}$ for a single junction cell [26, 38, 39]. The need for such a high energy means that silicon, which is an obvious choice for solar cells with its band gap of $1.14\,\mathrm{eV}$ close to the optimal efficiency, cannot be directly used for water splitting cells. In addition to its low bang gap, silicon also forms insulating silicon dioxide layer in presence of oxygen, which makes it unsuitable for oxygen evolution.

The required resistance to corrosion makes metal oxide semiconductors such as TiO_2 or Cu_2O good candidates for photoanodes as they are already oxidized and will not react with the oxygen. TiO_2 has been shown to have good catalytic properties leading to low overpotentials, especially with metallic co-catalyst or dye extending its absorption range. [40]. The high band gap allows good band edge positions, but results in poor photoconversion efficiency. Figure 8 shows how only a small fraction of the solar photon flux lies at energies that TiO_2 cell can utilize. In addition, the low carrier mobility limits the useful layer thickness due to increasing recombination losses. As expected from a metal oxide, TiO_2 has been shown to be chemically stable in aqueous electrolytes [41]. Other materials proposed include for example Fe_2O_3 (hematite) [42], CuO2 with TiO_2 overlayers [43] and even silicon despite its low band gap [17]. Silicon has a clear advantage as being an economical choice, but the low band gap severely limits the available voltage range. Therefore, silicon cannot be used to drive full water splitting reaction without external potential source.
For the work in this thesis, GaAs was chosen as the electrode material. It has good electron mobility which should limit recombination losses even with thicker electrodes [26], but suffers from poor corrosion resistance[41]. The corrosion issue can be mitigated by adding a protective layer on top of the electrode, that prevents direct contact between the GaAs and the electrolyte. The band gap is only slightly higher than the minimum 1.23 V required, which is why a single–junction GaAs–based electrode is not expected to be efficient driving the full water splitting reaction. The major benefit from using GaAs is that it allows for easy engineering of the doping levels and additional layers via metalorganic vapour phase epitaxy (MOVPE), with the eventual goal being a multilayer device capable of stand–alone water splitting, shown in fig. 12 d. Even if the single layer samples fabricated for this thesis do not produce sufficient photovoltage to drive the full water splitting reaction, they can be characterized by supplying additional bias voltage from the potentiostat used for the measurements.

2.10 Efficiency of a PEC cell

Generally, the efficiency of any system is defined as the ratio of the total output power to the input power. In the case of a PEC cell, the commonly used efficiency figure is the solar-to-hydrogen efficiency, which is the ratio of input solar power to the effective power produced as hydrogen fuel. This definition becomes problematic if the cell requires applied electrical power in addition to the solar radiation, as as is the case with the GaAs cells studied in this thesis. In order to characterize the effectiveness of the cell, the power supplied by the potentiostat at the operating point has to be taken into account. The solar-to-hydrogen efficiency is calculated as

$$\eta_{STH} = \frac{J \cdot 1.23\,[\mathrm{V}]\eta_{elec}}{P_s}, \tag{2.30}$$

where η_{STH} is the solar-to-hydrogen efficiency, J the operating current density, and P_s the input solar power density. η_{elec} is the Faradaic efficiency, which is the ratio of the

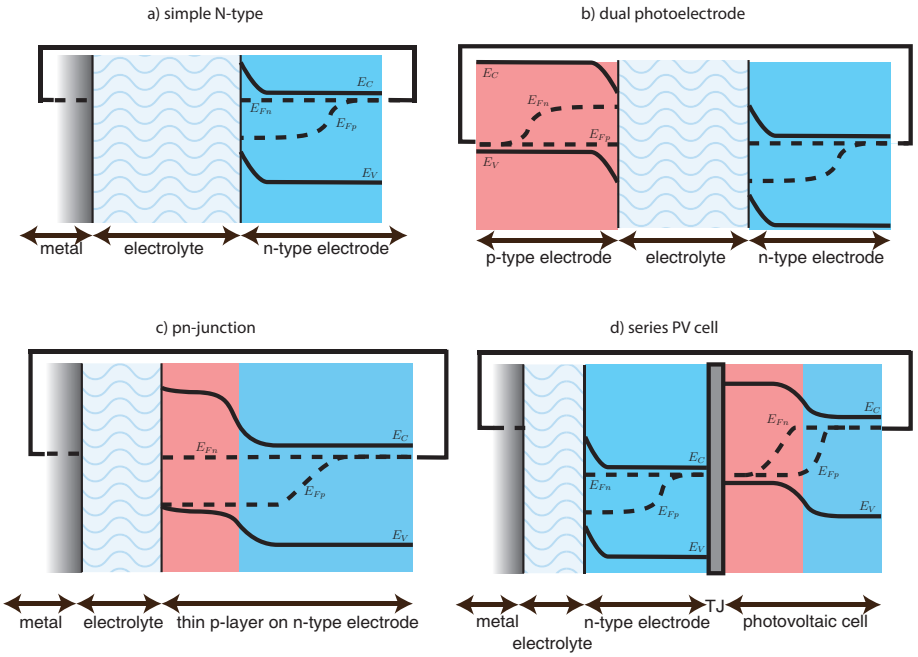

Figure 12: Different configurations of photoelectrochemical cells with pn junctions. a) is the simple, single doped semiconductor type. b) shows n–type photoanode and p–type photocathode connected to increase the overall usable voltage. c) is a buried pn–junction cell, which does not significantly increase the photovoltage, but might result in better charge transport efficiency at the SEI [33, 34]. d) is the eventual goal of the research this thesis is based on, a structure with a photovoltaic cell connected in series via a tunnel junction in order to generate sufficient photovoltage to drive the water splitting reaction without external bias.

total cell current to the current associated with the electrolysis reaction. For water splitting cells the faradaic efficiency can be assumed to be 1 [44]. If the cell cannot produce the voltage required to drive the reaction, the constant 1.23 V in eq. (2.30) has to be replaced with the voltage that is saved by using the photoelectrode instead of a non–photosensitive electrode. This dark reference (not to be confused with the reference electrode used for the three–electrode measurement setup) could be for example a metallic electrode, or the semiconductor electrode itself in dark conditions. In this work, an ideal electrode, which is able to drive the relevant reaction with zero overpotential, is used as the reference. This allows the calculation of the power saved–efficiency [44]. For n–type cells

$$\eta_{STHsaved} = \frac{J \cdot (V_{ref} - E_{red}^{RHE})\eta_{elec}}{P_s}, \tag{2.31}$$

where E_{red}^{RHE} is the reaction potential of the relevant evolution reaction. For p–type cells the sign of the difference between the reaction potential and V_ref has to be changed.

3 Simulation

This section will explain the mathematical methods used to implement the numerical simulation of a PEC cell, and present the key results obtainable from the simulations. The model combines the drift–diffusion equations within the semiconductor and the Gerischer model from eqs. (2.20) and (2.21) for the SEI currents. The simulation is also capable of modelling a buried pn–junction within the semiconductor in addition to the electrolyte interface.
The drift-diffusion model used for the system consists of six equations [45]. The definitions for current directions used in this thesis differ from those in [45], so the equations have been adjusted accordingly. In the formulation used in this thesis, the system is solved for electron and hole fluxes instead of electric current contributions, so that both electron and hole currents are positive when the respective charge carriers are flowing in positive x-direction. These currents then have opposite effects on the actual electric current of the photoelectric cell.

As mentioned already in section 2, the currents in the system are composed of drift and diffusion currents. These are defined separately for both charge carrier types in the following equations

$$j_p = qn\mu_p\mathcal{E} - qD_p\frac{\partial p}{\partial x}, \tag{3.1a}$$

$$j_n = -qp\mu_n\mathcal{E} - qD_n\frac{\partial n}{\partial x}, \tag{3.1b}$$

where q is the elementary charge, μ_p and μ_n are the carrier mobilities, and D_p and D_n are the diffusion constants. The drift currents caused by the electric field are to opposing directions for holes and electrons. The diffusion is towards the negative gradient for both, so that the carriers tend to flow from higher concentration region to lower.
The carrier fluxes are related to the net generation rate via the continuity equation. The general continuity equation for any transport system is

$$\frac{\partial\rho}{\partial t} + \nabla\cdot j = \sigma, \tag{3.2}$$

where ρ is the density of the quantity to be transported, j is the flux of the quantity and σ is the net generation rate. In the case of a one dimensional steady state model the time derivatives of the carrier densities are zero, so the continuity equations for the charge carriers can be written as

$$\frac{1}{q}\frac{\partial j_p}{\partial x} - G(x) + R(x) = 0, \tag{3.3a}$$

$$\frac{1}{q}\frac{\partial j_n}{\partial x} - G(x) + R(x) = 0, \tag{3.3b}$$

where $G(x)$ is the carrier photogeneration rate and $R(x)$ the recombination rate. The recombination model used is the simple, direct band to band recombination of

excess carriers

$$R(x) = \frac{1}{N_{A,D}\tau}\left(n(x)p(x) - n_i^2\right), \tag{3.4}$$

where $N_{A,D}$ is the doping density of the semiconductor, τ the lifetime of the minority carriers and n_i the intrinsic carrier density, defined as the product np in thermal equilibrium.
The carrier generation rate $G(x)$ in eqs. (3.3a) and (3.3b) is calculated by integrating the illumination spectrum from zero wavelength to the band gap of the working electrode material. For this work, the AM1.5G solar spectrum shown in fig. 7 and the spectrum of the lamp used for the experimental study were used. The incident photon flux is calculated from the power spectrum by

$$\Phi(\lambda) = \frac{P(\lambda)}{E_p(\lambda)}, \tag{3.5}$$

where $\Phi(\lambda)$ is the incident photon flux per area per wavelength, $P(\lambda)$ the incident power per area per wavelength (spectral irradiance) and $E_p(\lambda)$ the energy of a photon at the corresponding wavelength. The total absorbed photon flux is then the result of the integral

$$\Phi_a = \int_0^{\lambda_G} \Phi(\lambda) d\lambda, \tag{3.6}$$

where λ_G the wavelength corresponding to the band gap of the semiconductor and Φ_a the absorbed photon flux per area. The number of photogenerated electron–hole pairs is then calculated using the Beer–Lambert law

$$G(x) = \alpha \Phi_a e^{-\alpha x}, \tag{3.7}$$

where α is the absorption coefficient of the semiconductor and x the distance from the illuminated surface into the semiconductor.
The electric field within the system is related to the carrier densities via Poisson's equation

$$\frac{\partial \mathcal{E}}{\partial x} = \frac{q}{\varepsilon}(p - n + N_D - N_A), \tag{3.8}$$

where $\varepsilon = \varepsilon_0 \varepsilon_r$ is the permittivity of the material. Finally, an equation relating the electric field to the electrostatic potential within the semiconductor is needed

$$\mathcal{E} = -\frac{\partial \phi}{\partial x}. \tag{3.9}$$

The eqs. (3.1), (3.3), (3.8) and (3.9) form the complete drift–diffusion model to be solved, and will be referred to as the system equations. They have six dependent variables that are unknown functions of the spatial coordinate x. x is defined to be zero at the SEI (semiconductor-electrolyte interface). The system variables to be solved are:

- $p(x)$: hole density
- $n(x)$: electron density
- $j_p(x)$: hole current
- $j_n(x)$: electron current
- $E(x)$: electric field
- $\phi(x)$: electric potential

In addition to the system equations, boundary conditions are required. The boundary conditions in eqs. (3.10) are identical for all cell types, with effective current direction being determined by the overpotentials caused by the quasi–Fermi level positions at the SEI.

$$j_0^p e^{\frac{\eta_p}{V_{th}}} + j_p(0) = 0, \tag{3.10a}$$
$$j_0^n e^{\frac{-\eta_n}{V_{th}}} + j_n(0) = 0, \tag{3.10b}$$
$$\phi(0) + V_{SC} - \phi_0 = 0, \tag{3.10c}$$
$$qr_s\left(p(d) - p_{0i}\right) - j_p(d) = 0, \tag{3.10d}$$
$$qr_s\left(n(d) - n_{0i}\right) - j_n(d) = 0, \tag{3.10e}$$
$$\phi(d) - \phi_0 = 0, \tag{3.10f}$$

where j_0 are the exchange current densities for the carriers, V_{SC} is the electrostatic voltage drop across the semiconductor, r_s the back surface recombination rate, n_i the intrinsic carrier concentration of the semiconductor and ϕ_0 the electrostatic potential at the back contact. d is the sum of the layer thicknesses, which is the x-coordinate of the back surface.
Equations (3.10a) to (3.10c) define the boundary conditions at the SEI. A commonly used boundary condition for the charge transport across the SEI is based on a transfer rate constant, where the current is related to the amount of excess carriers at the interface [8, 18, 46].

$$j_n + qk_{tr}(n(0) - n_{dark}(0)) = 0, \tag{3.11}$$

Where k_{tr} is the transfer rate constant, $n(0)$ is the electron density at the interface, and $n_{dark}(0)$ the electron density at the interface at the dark equlibrium state. This model, however fails to account for the difference between the equilibrium potential E_{redox}, and the reaction potentials E^0_{red} from eqs. (2.13) to (2.16). In this work, instead of using the transfer rate constant, the current is related directly to the overpotential η shown in fig. 2 via the Gerischer model eqs. (2.20) and (2.21). As the relation between the carrier density and the quasi–Fermi level is exponential as seen in eqs (2.12), the boundary condition is effectively the same, with the addition

of accounting for the potential barrier required to reach the reaction potential. The free parameter k_{tr} is replaced with the exchange current density j_0.

The electrostatic potential at the SEI is the sum of the back contact potential and V_{SC}. The conditions at the back contact are explained by eqs. (3.10d) to (3.10f). The surface recombination rate r_s depends on the characteristics of the back junction. At an ohmic contact there should be no excess carriers, which can be modeled with a sufficiently high surface recombination rate.

In the case of a buried pn–junction, all six system variables are simply required to be continuous across the junction. The only exception is the electric field $\mathcal{E}(x)$, which will have a discontinuity in heterojunctions of materials with different permittivities.

3.1 Analytic model for the dark equilibrium

Before the drift–diffusion equations can be solved, the dark carrier concentrations, the carrier generation rate and V_{SC} must be known. In order to relate the simulation to the experimental work, the simulation controls the potential between the sample back surface Fermi level and the RHE in the electrolyte. The photocurrent can then be solved as a function of the voltage vs. RHE V_{ref} and illumination. The relation between V_{ref} and V_{SC} can be seen from fig. 2. The dark carrier concentrations are solved analytically using depletion region approximation at both the SEI and the pn–junction.

$$n(x) = n_0 e^{q(\phi(x)-\phi(d))/V_{th}} \tag{3.12}$$

$$p(x) = p_0 e^{q(-\phi(x)+\phi(d)/V_{th}}, \tag{3.13}$$

$$\phi(x) = \phi(d) - sign(V_{SC})\frac{qN_d}{2\varepsilon}(w-x)^2, \tag{3.14}$$

where w is the width of the depletion region

$$w = \sqrt{\frac{2\varepsilon}{qN_d|V_{SC}|}}. \tag{3.15}$$

The potential drop across the semiconductor is calculated from the energy diagram in fig. 2. For example for n-type semiconductor electrodes

$$V_{SC} = -V_H - \frac{1}{q}(\chi - \zeta) + V_{ref}. \tag{3.16}$$

For the buried junctions the potential across the pn–junction is assumed to be equal to the built in potential

$$V_{bi} = V_{th} \ln \frac{N_d N_a}{n_i^2}, \tag{3.17}$$

and the rest of V_{SC} is across the space–charge layer at the SEI. This allows the forming of an initial solution in the dark equilibrium used as a starting point for the numerical solver.

3.2 Numerical solver

The system is solved using a built in MATLAB general purpose boundary value problem (BVP) solver *bvp5c*, that implements the four stage Lobatto IIIa formula[47]. The formula is an implicit Runge-Kutta method, and as such it is able to solve moderately stiff problems such as the drift-diffusion systems in this thesis. The solver works by evaluating the derivatives of the system variables at collocation points, so the system equations eqs. (3.1), (3.3), (3.8) and (3.9) have to be rewritten with the derivatives solved

$$\frac{\partial n}{\partial x} = -\frac{1}{qD_n} j_n + \frac{\mu_n}{D_n} n\mathcal{E}, \tag{3.18a}$$

$$\frac{\partial p}{\partial x} = -\frac{1}{qD_p} j_p - \frac{\mu_p}{D_p} p\mathcal{E}, \tag{3.18b}$$

$$\frac{\partial j_n}{\partial x} = q(-G + R), \tag{3.18c}$$

$$\frac{\partial j_p}{\partial x} = q(G - R), \tag{3.18d}$$

$$\frac{\partial E}{\partial x} = \frac{q}{\varepsilon}(p - n + N_D - N_A), \tag{3.18e}$$

$$\frac{\partial \phi}{\partial x} = \mathcal{E}. \tag{3.18f}$$

The dependent variables of the system have a wide dynamic range of absolute values when represented in SI units ranging from carrier densities at up to $\mathcal{O}\ 10^{28}\,\mathrm{m}^{-3}$ to current densities around $\mathcal{O}\ 10^{-10}\,\mathrm{A/m}^2$. In order to make the system numerically stable and solvable, the problem is presented in a nondimensional form, where the dimensional quantities are scaled with intrinsic properties of the system. For example all carrier densities are divided by the doping density of the material to give a value with dimensionless units of m^3/m^3. In other words, the system is scaled to use 'one doping density' as a unit of density, which brings the numerical value of the density represented in the dimensionless form much closer to unity than the original value in SI units.

The process begins by figuring out the dimensions of all variables of the system. In this case there are a total of seven variables with five different dimensions, which are presented in table 3 with their conventional units. Before the nondimensionalization each variable is scaled to SI base units. It is easiest to begin with the independent variable x. A new variable x' is defined as

$$x' = \frac{x}{C_x}, \tag{3.19a}$$

$$\frac{\partial}{\partial x} x' = \frac{1}{C_x}, \tag{3.19b}$$

where x is the original variable in meters, C_x is the chosen characteristic length in meters and x' is the new dimensionless variable. All the other variables are functions of x, so in addition to scaling, the new dimensionless variables have to be written as

Table 3: Variables of the drift-diffusion model

Symbol	Variable	unit	Dimension
x	distance from SEI	nm	length
p	hole concentration	cm^{-3}	length^{-3}
n	electron concentration	cm^{-3}	length^{-3}
j_p	hole current	$\mathrm{A/cm}^2$	current $\times$ length^{-2}
j_n	electron current	$\mathrm{A/cm}^2$	current $\times$ length^{-2}
E	electric field magnitude	V/m	voltage $\times$ length^{-1}
ϕ	electric potential vs. back surface	V	voltage

functions of x' instead. In addition to the variables, the system also contains their differentials with respect to x. Equations (3.20) show the scaling of the hole density, but the process is identical for all the variables.

$$p'(x') = \frac{p(x)}{C_p} \Leftrightarrow p(x) = C_p p'(x'), \tag{3.20a}$$

$$\frac{\partial}{\partial x} p(x) = \frac{\partial}{\partial x} C_p p'(x'). \tag{3.20b}$$

Taking the constant out of the right hand side differentiation and applying the chain rule to eq. (3.20b) gives eq. (3.21a).The other derivatives are solved similarly.

$$\frac{\partial}{\partial x} p(x) = C_p \frac{\partial}{\partial x'} p'(x') \frac{\partial}{\partial x} x' = \frac{C_p}{C_x} \frac{\partial}{\partial x'} p'(x'), \tag{3.21a}$$

$$\frac{\partial}{\partial x} n(x) = \frac{C_p}{C_x} \frac{\partial}{\partial x'} n'(x'), \tag{3.21b}$$

$$\frac{\partial}{\partial x} j_p(x) = \frac{C_j}{C_x} \frac{\partial}{\partial x'} j_p'(x'), \tag{3.21c}$$

$$\frac{\partial}{\partial x} j_n(x) = \frac{C_j}{C_x} \frac{\partial}{\partial x'} j_n'(x'), \tag{3.21d}$$

$$\frac{\partial}{\partial x} E(x) = \frac{C_\mathcal{E}}{C_x} \frac{\partial}{\partial x'} E'(x'), \tag{3.21e}$$

$$\frac{\partial}{\partial x} \phi(x) = \frac{C_\phi}{C_x} \frac{\partial}{\partial x'} \phi'(x'). \tag{3.21f}$$

With the help of eqs. (3.19a) and (3.21), eqs. (3.18) can now be rewritten as

$$\frac{\partial p'}{\partial x'} = -\frac{1}{qD_p}\frac{C_j C_x}{C_p} j'_p + \frac{\mu_n C_x C_\mathcal{E}}{D_p} p'\mathcal{E}', \tag{3.22a}$$

$$\frac{\partial n'}{\partial x'} = -\frac{1}{qD_n}\frac{C_j C_x}{C_p} j'_n - \frac{\mu_n C_x C_\mathcal{E}}{D_n} n'\mathcal{E}', \tag{3.22b}$$

$$\frac{\partial j'_p}{\partial x'} = q\frac{C_x}{C_j}(G - R), \tag{3.22c}$$

$$\frac{\partial j'_n}{\partial x'} = q\frac{C_x}{C_j}(G - R), \tag{3.22d}$$

$$\frac{\partial \mathcal{E}'}{\partial x'} = \frac{C_x}{C_\mathcal{E}}\frac{q}{\varepsilon}(C_p(p' - n') + N_D - N_A), \tag{3.22e}$$

$$\frac{\partial \phi'}{\partial x'} = -\frac{C_x C_\mathcal{E}}{C_\phi}\mathcal{E}', \tag{3.22f}$$

and the boundary conditions from eqs. (3.10) as

$$j_0^p e^{\frac{\eta_p}{V_{th}}} - C_j j_p = 0, \tag{3.23a}$$

$$j_0^n e^{\frac{-\eta_n}{V_{th}}} - C_j j_n = 0, \tag{3.23b}$$

$$\phi(0) + V_{SC} - \phi_0 = 0, \tag{3.23c}$$

$$qr_s(C_p p(d) - p_{0i}) - C_j j_p = 0, \tag{3.23d}$$

$$qr_s(C_p n(d) - n_{0i}) - C_j j_n = 0, \tag{3.23e}$$

$$C_\phi \phi(d) - \phi_0 = 0. \tag{3.23f}$$

Equations (3.22) and (3.23) define the system that is supplied to the solver *bvp5c*. While the equations are not strictly speaking dimensionless, they have all the dimensions in the coefficients instead of variables. By assigning values to the scaling constants $C_x, C_p, C_j, C_\mathcal{E}$ and C_ϕ in their corresponding units the dimensions in the coefficients also cancel out. The numerical values of the scaling constants can be freely chosen to simplify the system. Ideally, the values of these parameters would not affect the solution as it is always scaled back to SI units using the same scaling constants in the other direction. However, due to limitations of floating point arithmetic, they do affect the accuracy, speed and stability of the numerical solver. For the case presented in this thesis trial and error with educated guesses was enough to find satisfactory values.

The basic idea behind solving a BVP numerically is to try and find a satisfactory approximation $S(x)$ of the true, unknown solution $y(x)$ by simultaneously minimizing the residual of the differential equations

$$r_d(x) = S'(x) - f(x, S(x)) \tag{3.24}$$

where $f(x, y)$ is the set of system equations, in this case eqs. (3.22), and the residual of the boundary conditions

$$r_b(x) = g(S(0), S(d)), \tag{3.25}$$

where $g(y(0), y(d))$ is the set of boundary conditions, in this case eqs. (3.23) [47]. The solver *bvp5c* does not use the residual as such directly, but instead the solver seeks a solution to

$$\Phi(X, Y) = 0, \tag{3.26}$$

where X is a mesh containing values of the independent variable x (the collocation points), Y contains the attempted solutions $S(x)$ at the mesh points defined in X, and Φ is a function for evaluating the error of the attempted solution, based on the definition of the residual. Φ can then be minimized by computing the global Jacobian

$$\frac{d\Phi}{dY}, \tag{3.27}$$

and using simple zero–finding schemes such as Newton's method. For detailed information about the numerical solver the reader is referred to the papers the authors of *bvp5c* have written about their solver and its predecessor *bvp4c* [47, 48]. A direct consequence of this type of error minimization is that the found solution will be a local minimum of the error function Φ. Therefore a reasonably good initial guess is required so that the solver converges to the correct solution. The nature of BVPs is that it is not apparent from the problem if there is a solution, or if there are infinitely many solutions. The quality of the initial guess is therefore extremely important for the performance of the solver. The initial solution is first calculated analytically for the dark equilibrium, which is then used a a starting point for the numerical solver. The solution is then extended by increasing the illumination in small steps, always using the solution from the previous step as the initial guess for the next step. This is a commonly used scheme when solving differential equations numerically called the continuation method. After a solution with full illumination is found, the same principle of continuation can be applied for varying any of the other parameters of the simulation such as the measured voltage V_{ref}.

3.3 Data analysis

After the solution is found, calculating the interesting quantities such as photovoltage and photocurrent is straightforward. The quasi–Fermi levels can be calculated with eq. (2.12), and the effective electrical current is the difference between the hole and electron currents. As seen in fig. 13, the simulator can reproduce results for the hematite cell studied in [18]. This is a reasonably strong confirmation that the model has been implemented correctly, and that the more generalized, overpotential based boundary conditions do agree with the simple transfer rate constant model used by [18].

The accuracy of the numerical method is ultimately limited by the double–precision floating point arithmetic used by the solver. The carrier densities can be almost constant over the bulk semiconductor and have rapid changes of up to ten orders of magnitude close to the interfaces. This results in a relatively stiff system. The Lobatto IIIa formula implemented in *bvp5c* is a collocation formula, that automatically adapts the collocation point mesh to fit the nature of the problem.

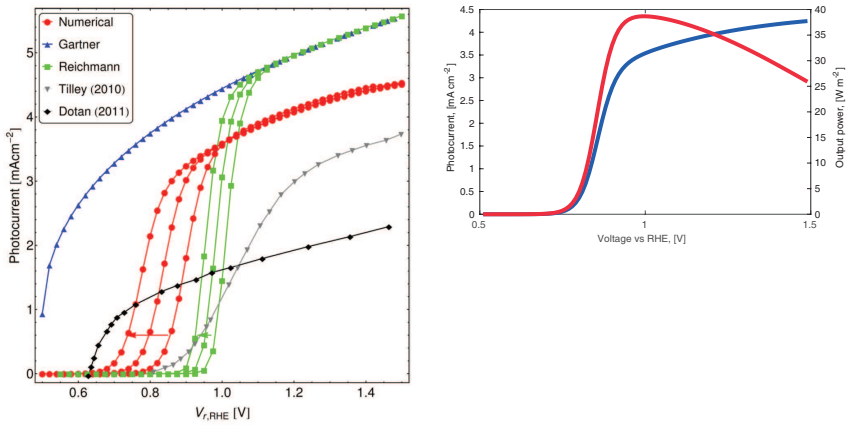

Figure 13: On the left numerical results by Cendula et al. in [18]. The curves labeled Gärtner [49] and Reichmann [50] are analytic models and Tilley [51] and Dotan [52] experimental results. On the right the result from the simulator implementaed in this thesis, with material parameters from [18], 33 nm of FeO_2.

The global error given by eq. (3.26) can be reduced not only by varying Y, but also by varying X. Increasing the mesh density around critical regions will mean that each element of Y has to approximate the solution for a shorter distance, thus reducing the error. The adaptive mesh is shown in fig. 14.

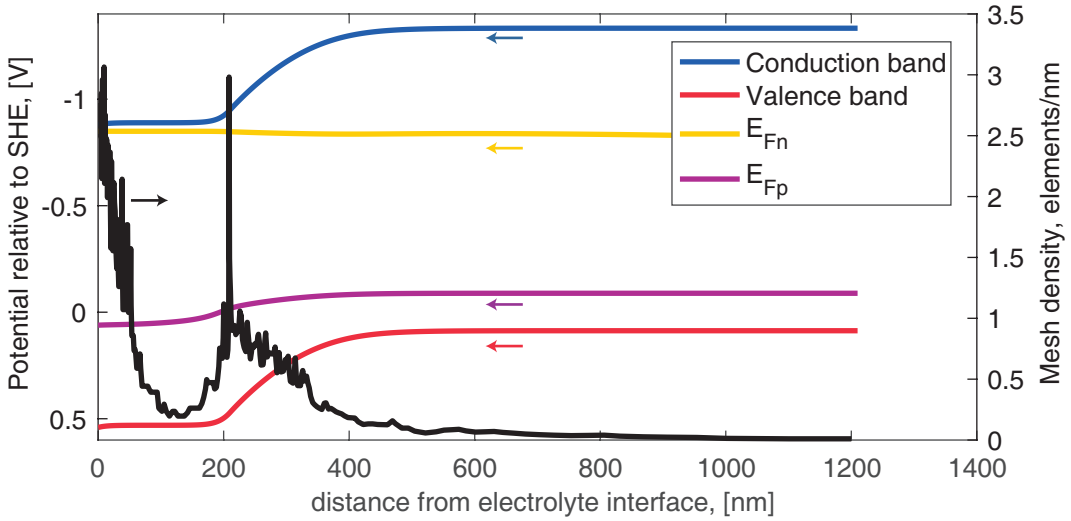

Figure 14: Example solution for 200 nm n–type GaAs on 1000 nm p–type. Higher mesh density is required at the SEI and at the pn–junction, where the carrier densities change rapidly. The peak at 200 nm is caused by a duplicate mesh point at the intermediate boundary at the pn–junction.

List of parameter values used for the simulations is given in table 4. the number of parameters needed for the simulation is large, and analyzing the complete parameter space is not a reasonable effort. Depending on the system, the simulator can solve 1–5 datapoints per second running on Intel® Core™ i5–3570K processor @ 4.1 GHz. Mapping the whole parameter space for 19 parameters, with ten datapoints each,

the runtime would be on the order of 10^{19} seconds, or 10^{11} years. It is therefore important to figure out which parameters should be varied, and what values the constant parameters are set to. For this work, the material parameters were held constant at literature values, and the focus was on simply verifying the current–voltage response against measured data.

Table 4: Parameters required for the simulation

symbol	parameter	value
	Material parameters	
χ	electron affinity	$4.07\,\mathrm{V}$
ε_r	relative permittivity	$12.9\,\mathrm{Fm^{-1}}$
E_g	band gap	$1.42\,\mathrm{eV}$
α	absorption coefficient	$5 \times 10^4\,\mathrm{cm^{-1}}$
V_{fb}	flat band voltage	measured
d	layer thickness	varied
	Charge carrier parameters	
N_D, N_A	doping density	varied
N_C	density of states for electrons	$4.7 \times 10^{17}\,\mathrm{cm^{-3}}$
N_V	density of states for holes	$9.0 \times 10^{18}\,\mathrm{cm^{-3}}$
μ_n	electron mobility	$8000\,\mathrm{cm^2V^{-1}s^{-1}}$
μ_p	hole mobility	$320\,\mathrm{cm^2V^{-1}s^{-1}}$
D_n	electron diffusion constant	$200\,\mathrm{cm^2s^{-1}}$
D_p	hole diffusion constant	$10\,\mathrm{cm^2s^{-1}}$
τ_n	electron lifetime	$5\,\mathrm{ns}$
τ_p	hole lifetime	$3 \times 10^4\,\mathrm{ns}$
j_0	exchange current density	varied
	External parameters	
pH	electrolyte pH	varied
V_{ref}	voltage against RHE	varied
P	illumination power	$500\,\mathrm{Wm^{-2}}$

4 Research material and methods

This section will describe the methodology used for the experimental work. First, the methods and materials used for sample fabrication are presented. For the work in this thesis, three different sample types were studied. The operating principles of the equipment used for the electrochemical measurements are explained, and finally the measurements taken are listed.

4.1 Fabrication methods

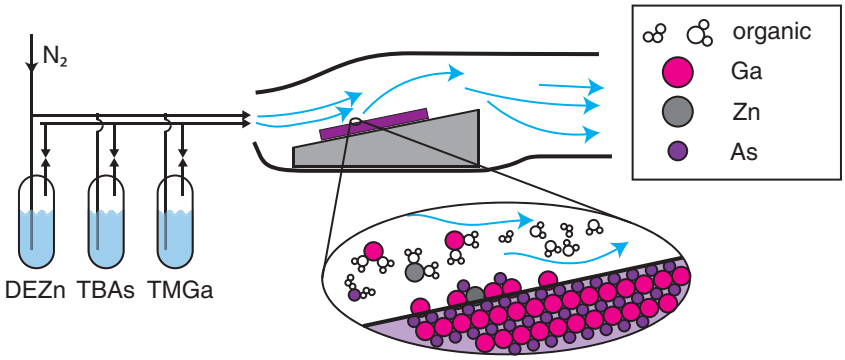

Figure 15: Working principle of MOVPE. When growing an n–type layer, the added zinc impurities replace gallium atoms in the crystal and act as electron donors. The precursor used for growing n–type GaAs are diethylzinc $(C_2H_5)_2$ Zn, tertiarybutylarsine C_4H_{11}As and trimethylgallium $(CH_3)_3$ Ga.

The samples were fabricated using doped GaAs wafers as substrate. Before any fabrication processes the samples were cleaned by rinsing first with acetone, then with isopropanol (IPA) and finally de–ionized water (DIW). Any residual water was dried with a nitrogen gun. The buried pn–junctions were made by growing a layer of n–doped GaAs on top of p–type wafer using MOVPE. The name of the method describes the growth mechanism: the precursors contain the metal atoms to be deposited in molecules with organic groups. These precursors flow over the sample as vapour in the inert carrier gas, and react on the surface depositing the metal atoms as a continuation of the original surface crystal structure. The organic parts of the precursors are then carried away in the exhaust. The operation principle for n–doped layer growth is shown in fig. 15: the carrier gas (N_2) is bubbled through the liquid precursors. The flow rates of each precursor are controlled separately, and the resulting vapour mixture is then carried through the reactor chamber. MOVPE is an efficient method for fabricating doped layers of III–V semiconductors as the dopants are directly included during the growth process removing the need for additional doping process step.

The protective TiO_2 layer was added on using atomic layer deposition (ALD). The operating principle of ALD is similar to MOVPE in that the growth material is carried to the sample by vapour phase precursors, but there are several key differences. In MOVPE, all precursors flow through the reactor chamber simultaneously, driving

continuous growth of the deposited layer. In ALD, the precursors are used sequentially, purging the reactor in between exposures to the different precursors. The precursors are chosen so that they only react with the opposite material at the surface, for example in case of TiO_2 deposition the titanium will only attach to the oxygen atoms at the surface, without growing a continuous titanium layer. By alternating the exposure to the precursors the film thickness can optimally be controlled within the thickness of one atomic layer. This makes ALD a lucrative choice for depositing extremely thin films on the order of 10 nm, as long exposure times can be used to ensure uniform film coverage without increasing the resulting film thickness.

All sample types were then coated with 10 nm of TiO_2 using ALD. Finally, back side ohmic contacts were fabricated by evaporating a 200 nm layer of indium directly on the samples. The indium coating was done by electron beam evaporation, where an electron beam emitted from a filament is directed at the metal target with magnetic field. The target material then evaporates and covers the sample surface. Evaporation was chosen as the deposition method out of personal preference, sputtering would just as valid option.

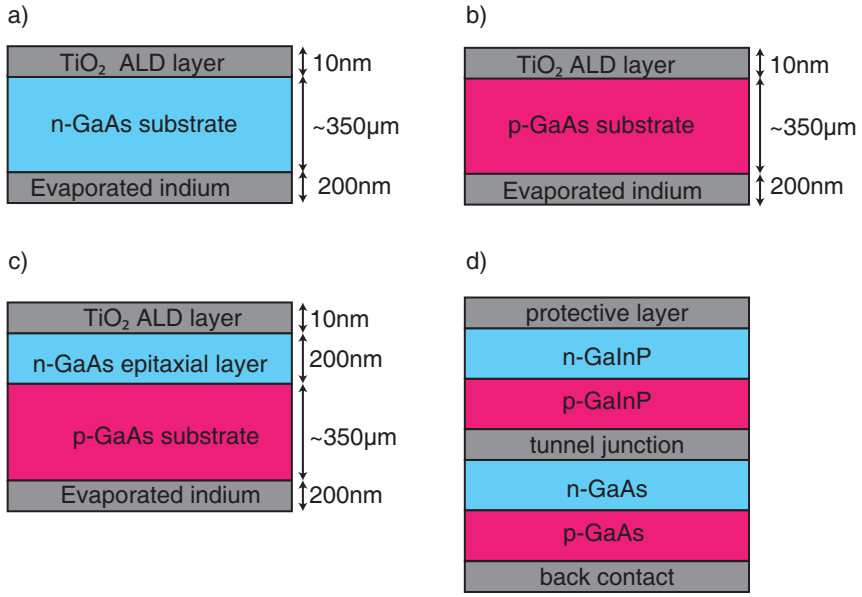

Figure 16: Cross sections of the fabricated samples. a) n–type sample, b) p–type sample, c) p–type sample with n–type epitaxial layer. d) is an example of the multi–junction structure that could drive the water splitting reaction without external voltage bias.

4.2 Measurement methods

All electrochemical measurements were made using 0.1M H_2SO_4 as electrolyte, which corresponds to pH $\approx$ 2. Before measurements the samples were cleaned using the same cleaning process as before the fabrication: rinsing first with acetone, then with IPA and finally with DIW. After the cleaning the samples were dried with N_2. The samples were then placed in the cell one at a time for measurements. The electrolyte solution was purged with nitrogen for 30 minutes before measurements to ensure

minimal amount of error from unknown amounts of dissolved hydrogen and oxygen. Figure 18 illustrates the used three–electrode setup and the cell. The sample is secured so that it is exposed to the electrolyte from the side onto which the active layers were fabricated. A rubber o–ring ensures a watertight seal. The reference and counter electrodes are then inserted into the electrolyte through the top of the cell. The main potentiostat controlling the measurement was *Zennium pro* from ZAHNER–elektrik. A secondary potentiostat, *PP211* from the same manufacturer, was used to control the illumination. The illumination control is done by utilizing a feedback photosensor placed next to the cell, within the light beam from the lamp. The feedback sensor was initially calibrated for the setup by using a calibration sensor with known response in place of the photoelectrochemical cell. The calibration allows the illumination to be controlled by directly specifying the desired power density at the sample, with the potentiostat automatically adjusting the driving current of the lamp based on the feedback signal. The intensity spectrum of the lamp is shown in fig. 17. Comparing the spectrum to the AMG1.5 spectrum from figs. 7 and 8 shows that the lamp can not be considered as a good solar simulator, since most of its radiation lies at wavelengths shorter than the band gap of GaAs. As a result the photocurrents measured at a set power density can be expected to be higher than if a solar simulator, or real sunlight, were used at the same power density.

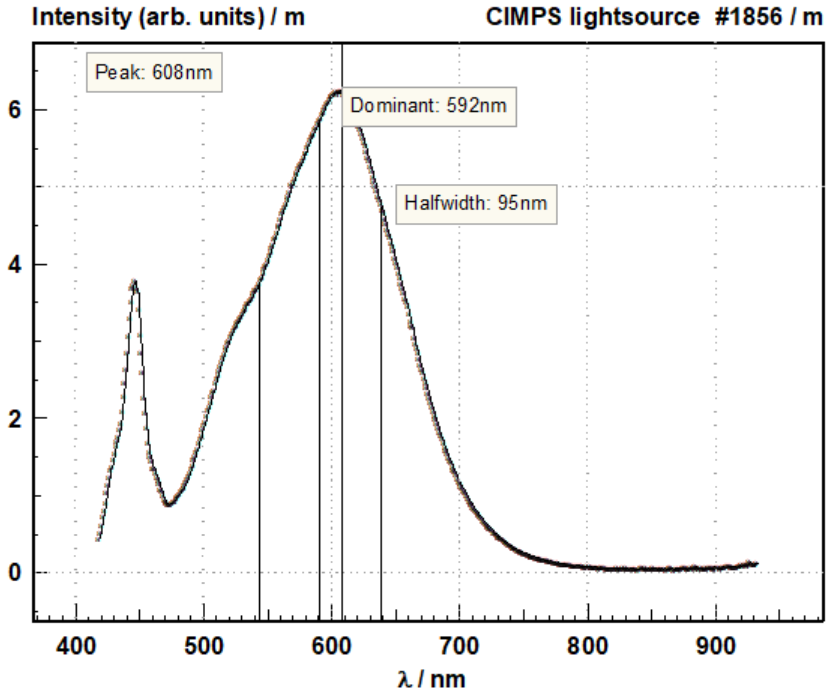

Figure 17: Intensity spectrum of the lamp used for the photoelectrochemical measurements, as provided by the manufacturer ZAHNER elektrik.

For potentiostatic measurements the current through the counter electrode is controlled to keep the voltage between the reference electrode and the working electrode, i.e. the sample, at a set value. The reference electrode used for the

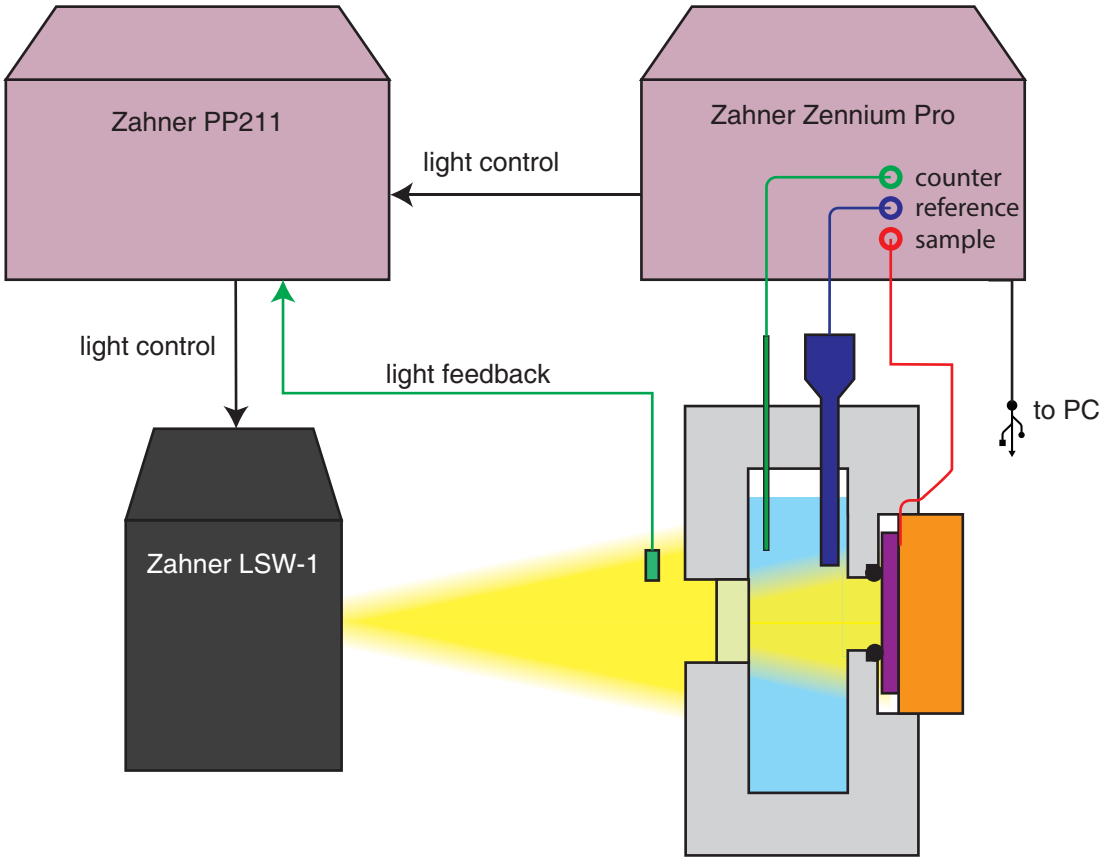

Figure 18: schematic of the measurement setup used with the potentiostat.

measurements was Gaskatel HydroFlex® RHE. The RHE will follow the hydrogen evolution potential shown in fig. 5. Since no current is allowed through the reference electrode, in steady state the current at the counter electrode is equal to the current at the working electrode. The measurements done for all samples included the following

- open circuit voltage
- chopped light voltammetry
- impedance spectroscopy.

Measuring the open circuit voltage is straightforward: the current at the counter electrode is set to zero and the voltage of the sample against the reference electrode is then measured. The measured voltage is the difference between the potential of the reference electrode and the equilibrium Fermi level at the rear surface of the sample. For voltammetry measurements the workstation adjusts the current at the counter electrode until the voltage of the working electrode vs. the reference electrode reaches the desired value. This is repeated for a range of voltages so that a current–voltage curve can be obtained. The voltammetry measurements were done under chopped illumination of $500\,\mathrm{Wm^{-2}}$, with six second cycle time. The voltage ramp rate used was $10\,\mathrm{mVs^{-1}}$, and the voltage range was varied between -1.5 and 1.5 V

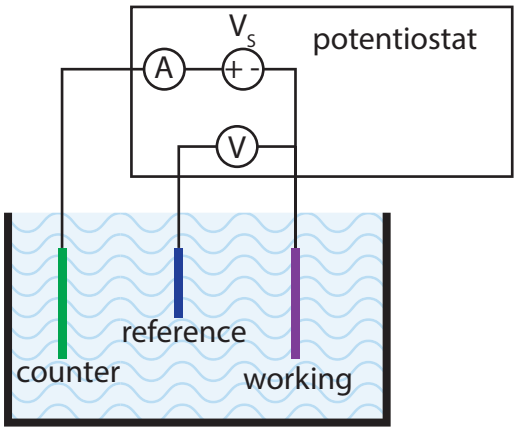

Figure 19: The principle of the three–electrode measurement: voltage is measured between the working electrode and the reference electrode, and current between the working electrode and the counter electrode.

depending on the sample. The chopped illumination allows the measurement of both the illuminated and dark currents at the same time, and the effective photocurrent can then be calculated as the difference from these two.

The electrochemical impedance spectroscopy (EIS) measures the impedance of the

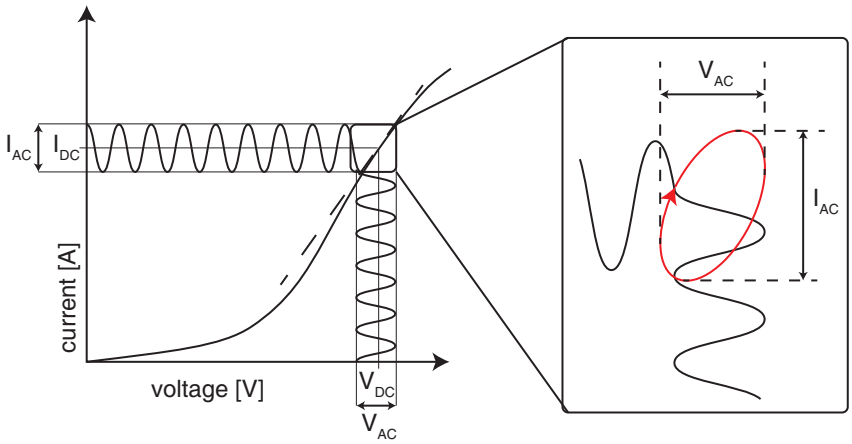

Figure 20: Illustration of the EIS measurement. The continuous line represents a typical nonlinear I-V response of a PEC cell. The dashed line is the linear extrapolation of the local differential resistance at the measurement point. The AC excitation causes the current–voltage curve to form an ellipse as shown in the inset. The arrow points the direction of the signal for capacitive loads.

cell as a function of input signal frequency. As shown in fig. 20, the operating point (V_{DC},I_{DC}) is set as in voltammetry measurements. A small amplitude AC signal is then added on top of the DC bias and the differential resistance

$$R_{diff} = \frac{|V_{AC}|}{|I_{AC}|}, \tag{4.1}$$

is measured. If the AC amplitude is small enough, the I–V curve can be locally approximated as linear (R is locally constant). From this approximation the impedance

can be calculated by

$$Z(f) \approx \frac{V_{AC}(f)}{I_{AC}(f)} e^{i\theta}, \tag{4.2}$$

where f is the frequency, V_{AC} is the AC voltage amplitude, I_{AC} is the AC current amplitude, and θ is the phase angle between the voltage and the current. [53]
The EIS measurements were done with a frequency range from 1 Hz to 1 MHz. The frequency step used was the default setting of the instrument, with 10 data points per decade at frequencies above 66 Hz and 5 steps per decade below it. The frequency sweep was repeated for voltages from -0.7 to 1 V for the n–type sample and -1 to 0.7 V for the p–type and buried np–junction samples. The voltage ranges were chosen based on the voltammetry measurements with the assumption that the flat band voltage should be close to the observed photocurrent onset voltage.

5 Results

The simulated results were computed using the parameters from table 4. For the simulations, the Helmholtz voltages were calculated from the measured flat band voltages with eq. (2.24). The cell thickness used was 800 nm for the one–layer cases. This is orders of magnitude lower than the actual thickness of the samples, which was roughly 350 µm. Even with the ability to adapt the mesh according to the solution, simulating a system with thousand times the size of the depletion region is not feasible with the numerical method used in this thesis. As both the chemical reactions and the light absorption happen at or close to the SEI, the added thickness excluded from the simulation is assumed to contribute a purely ohmic load to the system.
Another disparity between the simulation and the measurements is the doping densities of the semiconductors. The wafers used for fabricating the samples were very highly doped, at $1 \times 10^{18}\,\mathrm{cm}^{-3}$ for the n–type and $1 \times 10^{19}\,\mathrm{cm}^{-3}$ for the p–type. These densities are higher than the densities of states for electrons and holes in GaAs, and result in a degenerate semiconductor. The simulations were made with lower doping densities at $1 \times 10^{17}\,\mathrm{cm}^{-3}$ to ensure the validity of the Maxwell–Boltzmann statistics used in the derivation of the transport model.
Finally, the exchange current density was adjusted in order to get the best possible fit to the measured current–voltage response. The exchange current density mainly affects the required overpotential for photocurrent onset, and is limited by the requirement of the quasi–Fermi levels to stay $3k_BT$ inside the band gap.

5.1 Flat band voltages

Equivalent RC–circuits were fitted to the cell frequency responses acquired from the EIS measurements. The equivalent circuit models were fitted by minimizing the sum of squares of the residuals

$$r = \sum_{i=1}^{n} |Z'(\kappa, f_i) - Z(f_i))|^2, \tag{5.1}$$

where r is the total residual to be minimized, n the number of frequency points, Z' is the impedance transfer function of the equivalent circuit, κ a vector containing the fitting parameters, i.e. the values of the components of the circuit, f is the frequency vector, and Z is the measured complex impedance. The circuits used for the fitting are shown in fig. 21. The series resistor $R3$ corresponds to the total series resistance of the system. This resistance comes mostly from the electrolyte between the working and counter electrodes. The parallel RC–circuit formed by $R1$ and $C1$ models the resistance and the capacitance at the SEI, and $R2$ and $C2$ a secondary capacitive response detected in some measurements. This secondary capacitance could be from the Helmholtz layer, of from poor back side contact. Even if the source of the capacitance is uncertain, it has to be included in the model to ensure a good fit and to be able to extract the capacitance formed in the semiconductor space–charge

layer. However, the full five–element model could not be used in cases where the semiconductor capacitance dominates the response as the curve fitting converges to a solution with two roughly identical capacitance values instead of one dominating the other. This prevents the extraction of the semiconductor capacitance from the solution, so the simpler, three–element model was used instead when required.

Table 5: Flat band voltages

illumination	p–type	n–overlayer	n–type
$0\,\mathrm{Wm^{-2}}$	704 mV	−14 mV	237 mV
$500\,\mathrm{Wm^{-2}}$	271 mV	335 mV	−420 mV

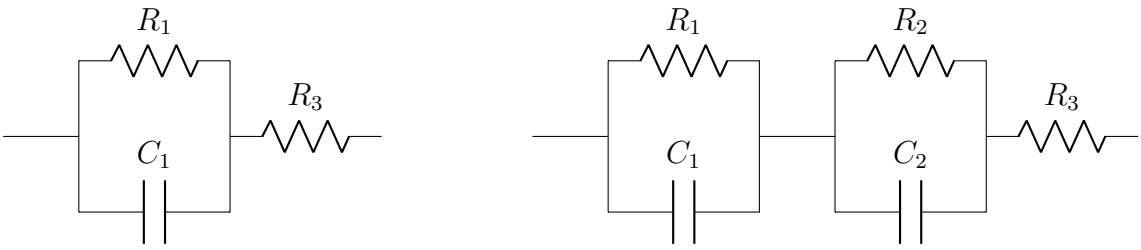

Figure 21: Equivalent circuit topologies tried used for extracting the capacitance. The simpler circuit on the left was used when the measured impedances were dominated by one capacitance.

5.2 P–type sample

The p–type sample is expected to act as a photocathode, driving the hydrogen evolution reaction at the SEI. In the 0.1M H_2SO_4 electrolyte the standard potential for the hydrogen evolution reaction is −0.12 V. The measured current should be negative when the electron quasi–Fermi level is more negative than the reaction potential. The Mott–Schottky plots in fig. 22 show a clear, linear relationship between the inverse square of the capacitance and the voltage. It is apparent, that the capacitance–voltage characteristics and the flat band voltage depend on the illumination. The slope is negative for both cases, as expected from a p–type sample. The slope of the linear fit to the measurements made in the dark corresponds to a doping density of $5.2 \times 10^{19}\,\mathrm{cm^{-3}}$, calculated from eq. (2.26). The value is quite high compared to the wafer specifications, but not entirely out of scope considering the inaccuracies in both the measurement and wafer manufacturing. In both the dark and illuminated cases a flat region is visible in the middle of the linear slope. This response confirms the presence of surface energy states within the band gap, which are not taken into account in the numerical model.

The measured current–voltage curve is shown in fig. 23. The photocurrent is clearly visible, but the overpotential required for the current to start is massive. The measured potential is the Fermi level at the back of the semiconductor, and the photovoltage generated in the semiconductor causes the electron quasi–Fermi level

to be even more negative. As the measured voltage is below the reaction potential when photocurrent is generated, the cell is less efficient than an ideal, externally powered electrolysis system. The measured power density in fig. 23 is the power saved compared to ideal electrode, which results in negative power density at voltages below the reaction potential.

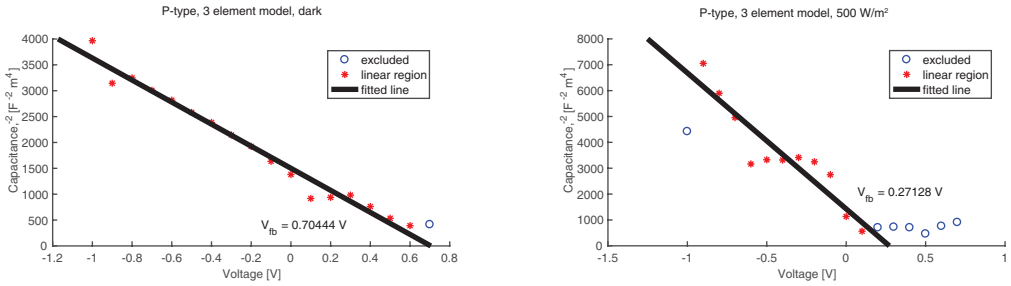

Figure 22: Mott-Schottky plots of p-type GaAs with TiO_2 coating using the three–element circuit. The flat band voltages were determined by extrapolating the linear fits.

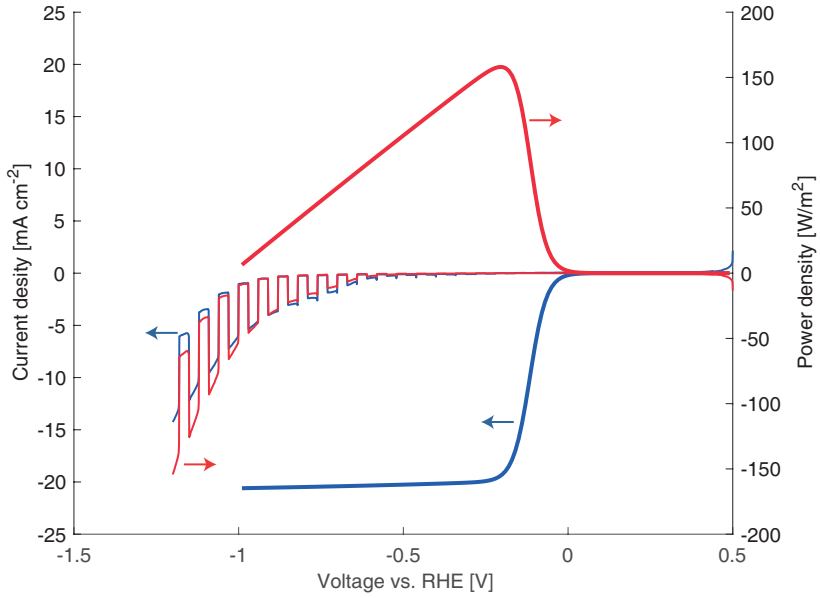

Figure 23: The measured current and power density (chopped curves) measured from the p–type sample compared to the simulated result (smooth curves).

The simulated response is drastically different. The simulator cannot account for the excessive overpotential shown in the experimental results. The simulated overpotential depends on the exchange current density for the conduction band reaction, which is a free parameter. Decreasing the exchange current density moves the simulated photocurrent onset towards more negative potentials, but at the same time it increases the carrier density required at the SEI to drive the current. Too low values of the exchange current density will quickly result in degenerate conditions at the SEI, which cannot be accurately explained by the simulation. The simulated saturation photocurrent magnitude is also observed to be much higher than the

measured current density.
The simulated carrier densities at the maximum power point are shown in fig. 24 a). The majority carrier density differs only slightly from the analytic solution for the dark equilibrium. However, the illumination causes large increase in the minority carrier density and forms an inversion layer at the SEI. Figure 24 b) shows the energy bands at the same operating point. The rear contact potential is at the quasi-Fermi level of holes at the back surface. The finite value used for the back surface recombination in eqs. (3.23d) and (3.23e) means that the simulated back contact is not perfectly ohmic, and the quasi–Fermi levels are not necessarily equal to each other. The effective photovoltage produced by the cell is the difference between the majority carrier quasi–Fermi level at the back surface, and the minority carrier quasi–Fermi level at the SEI. The figure also shows that the electron quasi–Fermi level at the SEI is very close to the conduction band. The simulated overpotential could be increased by reducing the exchange current density, but this would force the quasi–Fermi level inside the conduction band.

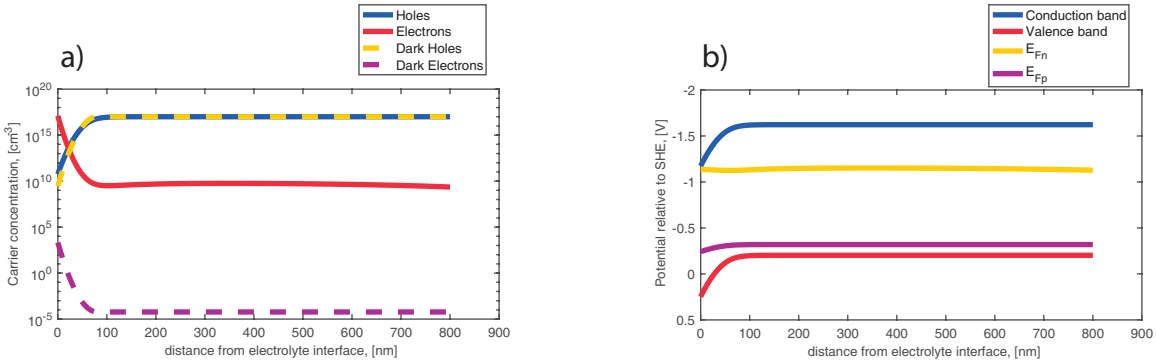

Figure 24: a) Carrier concentrations of the p–type electrode at the simulated maximum power point $V_{ref} = -0.20\,\mathrm{V}$. b) The energy bands at the same operating point.

5.3 Buried np–junction

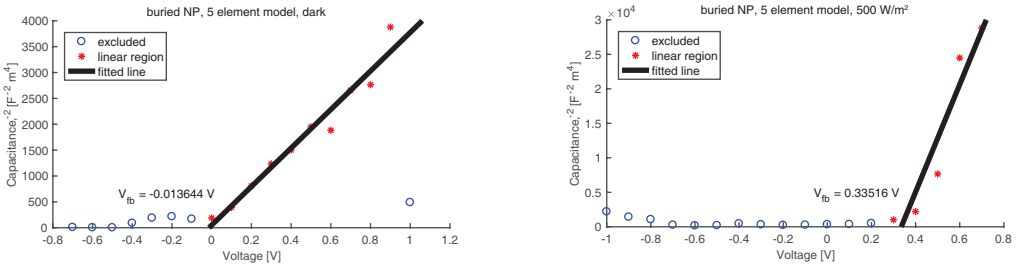

Figure 25: Mott-Schottky plot of p–type GaAs with n–type epitaxial layer and TiO_2 coating using the five–element circuit. The flat band voltage was determined by extrapolating the linear fit.

According to the theory explained in section 2, a photoelectrode with n–type epitaxial layer on top of p–type substrate should have a similar response as the simple p–type photoelectrode: the reactive carriers are electrons, and the net photocurrent

should be negative. Figure 26 shows that both the measured and the simulated systems have the expected photocurrent response. The current–voltage curves are quite similar to those of the p–type case, but both the simulated and the measured systems show a slight increase in the photocurrent magnitude. The simulated overpotential cannot be matched with the measured one for the same reason as the p–type case: it would require highly degenerate carrier density at the SEI. Figure 27 a) shows a slight accumulation layer at the SEI at the simulated maximum power point. In the energy band diagram shown in fig. 27 b) the band bending caused by the buried pn–junction is clearly visible. The Mott-Schottky plots in fig. 25 show n–type response at the SEI, confirming the theory for the effect of the epitaxial layer. The measured photocurrent increases towards negative potentials, where the Mott–Schottky plot is flat.

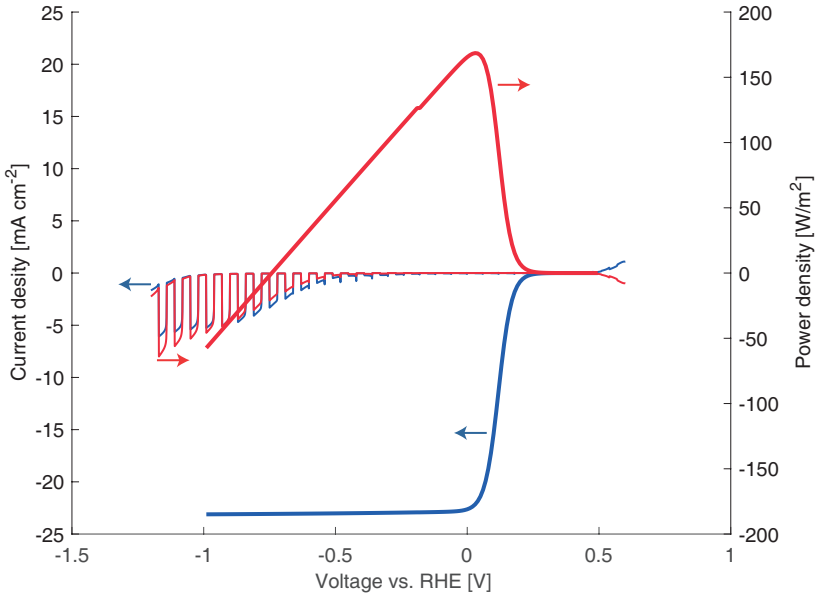

Figure 26: The measured current and power density (chopped curves) measured from the sample with the buried pn–junction compared to the simulated result (smooth curves).

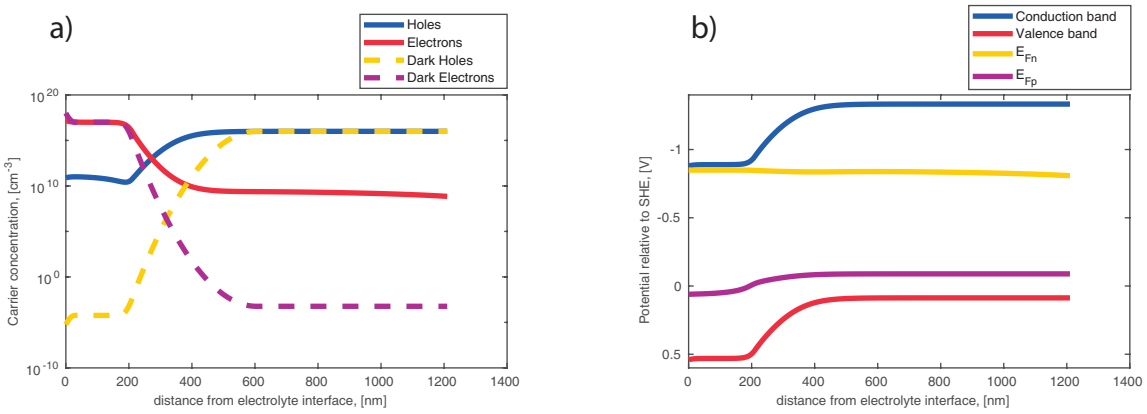

Figure 27: a) Carrier concentrations of the 200 nm n–type layer on p–type electrode at the simulated maximum power point $V_{ref} = 0.03\,\mathrm{V}$. b) The energy bands at the same operating point.

5.4 N–type sample

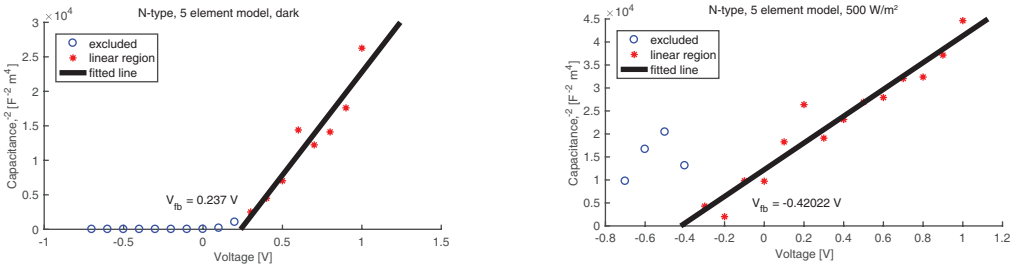

Figure 28: Mott-Schottky plot of n-type GaAs with TiO_2 coating using the five–element circuit. The flat band voltage was determined by extrapolating the linear fit.

According to the theory, the n–type sample should be capable of driving the oxygen evolution reaction, which requires the hole quasi–Fermi level to exceed the standard potential of the reaction. Therefore, the expected result is positive photocurrent increasing towards more positive measured voltage.

The measured photocurrent from the n–type sample shown in fig. 29 is significantly better than the one from the p–type. The curve in fig. 29 looks promising, and in this case the measured sample seems to be more efficient than the simulated device. However, comparing the power saved efficiency, calculated with eq. (2.31), of 15% from a simple, n–type cell to the state-of-the-art multi–layer device by Young et al. [7] that achieved efficiency of 16% suggests caution. Comparing the measured photocurrent onset at $-0.1\,\mathrm{V}$ against the oxygen evolution reaction potential for the measured system at roughly 1.11 V, implies a photovoltage of at least 1.2 V, not including the overpotential required for the reaction. The photovoltage predicted by the simulation, including the overpotential, is 0.9 V. It is possible that the reaction happening at the n–type electrode is not the oxygen evolution reaction, but corrosion of the GaAs. This implies failure of the protective TiO_2 layer, and should be verifiable by for example scanning electron microscopy of the used sample.

The simulated results for the n–type electrode are quite similar to those of the

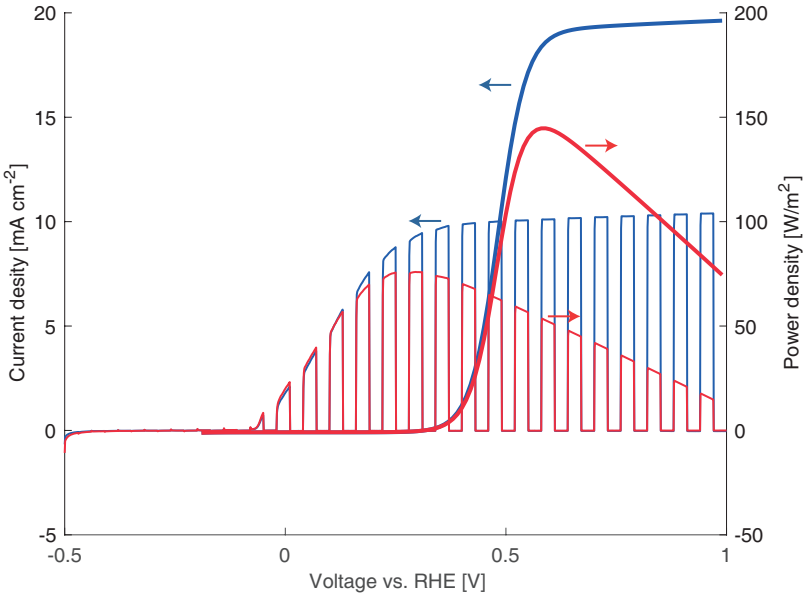

Figure 29: The measured current and power density (chopped curves) measured from the n–type sample compared to the simulated result (smooth curves).

p–type, with the difference of the current direction. These are expected results, as the simulations of the different electrode types differ only by the kinetic parameters, which mainly affect the required overpotential, and the different carrier transport parameters for electrons and holes. The carrier densities in fig. 30 a) show a similar inversion layer to fig. 24 a), only in the opposite direction. The energy band diagram in fig. 30 b) show the hole quasi–Fermi level at the SEI just barely exceeding the oxygen evolution potential of 1.11 V against the SHE. This means that the simulated overpotential is at its minimum, and the simulated photocurrent onset cannot be moved further to the negative direction by adjusting the kinetic parameters.

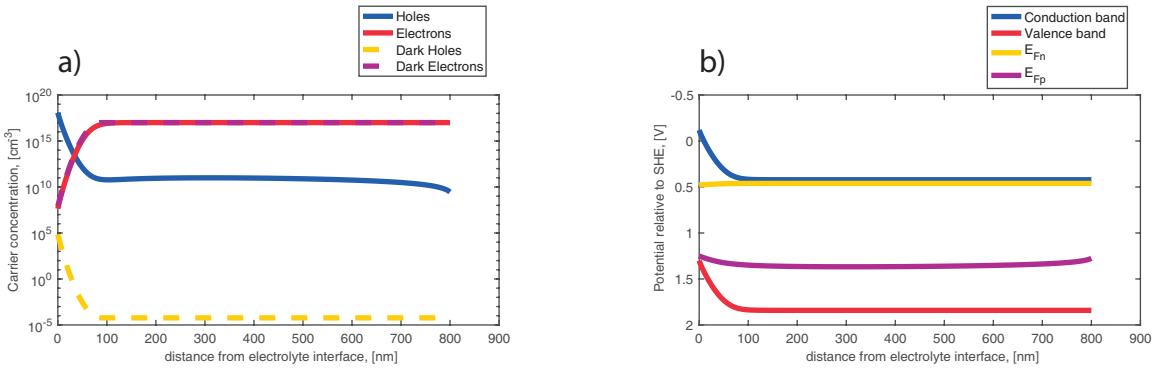

Figure 30: a) Carrier concentrations of the n–type electrode at the simulated maximum power point $V_{ref} = 0.58\,\mathrm{V}$. b) The energy bands at the same operating point.

5.5 Discussion

As can be seen from the presented results, the numerical model can predict the qualitative response of the system. The directions of the simulated photocurrents for all samples match the experimental results, but the simulation cannot account for the extreme overpotential that is required to drive the hydrogen evolution reaction. The simulated overpotential can be increased by decreasing the exchange current density, but this has the consequence of increased carrier density at the surface. Assuming that the measured flat band voltage is accurate, the measured current–voltage response corresponds to highly degenerate carrier densities, which cannot be accurately modeled with Maxwell–Boltzmann statistics. The simulation also takes the flat band voltage into account only as a constant value. However, the results indicate that the flat band voltage is not constant, but depends on the operating point of the cell. This would effectively lead to band edge unpinning, where the band edge positions, and the Helmholtz voltage, vary with the flat band voltage. While the flat region in the Mott-Schottky plots was only visible for the p–type sample, this was also the only sample for which a good impedance fit was achieved using the three–element equivalent circuit. The poor fit of the simple model to the sample with the buried junction was expected, as the pn–junction will have its own capacitance. For the n–type sample it is possible that the corrosion affected the measurement, as the runtime for the full EIS scan was over 30 minutes. This variation of the flat band potential could be explained by the presence of surface trap states, that allow carriers with energies inside the band gap at the SEI [54].

All the other parameters also have inaccuracies associated with them. For example, the carrier mobilities and diffusion coefficients are modeled as constant values. However, the electric fields at the SEI and the pn–junction can be of the order of 10 kV/cm, which is enough to cause drift velocity saturation and reduced mobility. This electric field dependence of the diffusion parameters should be taken into account for more accurate results.

It is also unclear, whether the effect of the protective TiO_2 layer can be ignored. Even if the layer is thin enough not to restrict charge carrier exchange between the GaAs and the electrolyte, it could well contribute to the amount and position of the surface states. The immediate surface layer of the electrode is also what mostly defines the catalytic properties of the electrode, and therefore the kinetics of the redox reactions. In this thesis, the kinetics are modeled with two parameters, namely the exchange current density and the flat band voltage. As all the measured samples shared the same TiO_2 overlayer, any effect caused by it is included in the kinetic parameters. For future development of the photoelectrochemical cell, the ability to quantify the effects of the TiO_2 layer would be helpful.

The recombination model used in the bulk semiconductor only accounts for direct band to band radiative recombination. Even though this should be the main recombination type in a direct band gap material such as GaAs, including other recombination models would improve the accuracy especially if the simulation is used for materials with indirect band gaps, such as silicon.

Changing the pH of the electrolyte will shift both the hydrogen and oxygen evolution

potentials according to fig. 5. The theory for the Helmholtz layer results in identical shift of the band edge positions given in eq. (2.23), so the pH value should have no direct effect on the energetics of the system. It will however affect the conductivity of the solution and whether the majority of the reactions at the electrodes will be with H^+ or OH^- ions. The ion concentration could have effect on the chemical stability of the electrode, so in general the effect of the electrolyte pH should be studied.

6 Conclusion

The implementation of the numerical model of the semiconductor electrode in a photoelectrochemical cell was successful. The simulator can solve the carrier densities, currents and the electric field in the semiconductor, and consequently model the current–voltage response. The model is general enough so that it works for both n– and p–type cells without changing boundary conditions, and can correctly predict the qualitative effect of a buried pn–junction. Comparison to experimental results shows, that the physical model behind the simulation is inadequate for quantitatively predicting the response of a real semiconductor electrode. The disparity between the simulated and measured response is most likely explained by the exclusion of surface phenomena from the model, such as surface trap states within the band gap and unpinning of the band edges.

The experimental results achieved suggest that p–type GaAs is not very efficient in driving the hydrogen evolution reaction. The most critical part to improve would be reducing the required overpotential. This could be done for example by adding co–catalyst nanoparticles on the electrode surface [15]. Adding the epitaxial n–type layer somewhat improves the result, but it is still less efficient than a good, metallic electrode that is not photoactive. However, the result is in line with the theory of thin, oppositely doped layer increasing the efficiency of a semiconductor photoelectrode. For the experimental work, the sample size in this work is too small to draw any strong conclusions. More measurements are needed to control for the effects of corrosion of the electrode, pH of the electrolyte and TiO_2 overlayer. Especially in the case of the n–type cell, assuming that the measured current for the n–type sample is due to corrosion and not water oxidation, a better solution for the protective layer is required.

In order to build a model that could reliably predict the response of a semiconductor photoelectrode, a better understanding of the surface interaction at the SEI is needed. This includes a model that could predict the band edge positions as function of both illumination power and voltage bias. In addition, the assumption of non–degenerate carrier densities is severely limiting. However, computing the Fermi–Dirac integrals numerically for each iteration during the solver run would be computationally too expensive.

Even though the simulator cannot accurately predict the response of a PEC cell, it shows potential for future development. Most of its shortcomings arise from simply excluding physical phenomena that have significant effects on the system. For the future development of the model, taking into account the effects of the surface states to the charge transfer between a semiconductor and electrolyte should be considered [46, 55]. The results could also be improved by better modeling of the carrier transport in degenerate semiconductors [56], or by including charge diffusion in the electrolyte [57]. Regardless of its inaccuracy, the simulation can already offer insight into the internal dynamics of a PEC cell, and it will be a useful tool in the continued research of the cells.

References

[1] P. Nikolaidis and A. Poullikkas, "A comparative overview of hydrogen production processes", *Renewable and sustainable energy reviews*, vol. 67, pp. 597–611, 2017.

[2] J. Newman, P. G. Hoertz, C. A. Bonino, and J. A. Trainham, "An economic perspective on liquid solar fuels", *Journal of The Electrochemical Society*, vol. 159, no. 10, A1722–A1729, 2012.

[3] M. R. Shaner, H. A. Atwater, N. S. Lewis, and E. W. McFarland, "A comparative technoeconomic analysis of renewable hydrogen production using solar energy", *Energy & Environmental Science*, vol. 9, no. 7, pp. 2354–2371, 2016.

[4] A. Rothschild and H. Dotan, "Beating the efficiency of photovoltaics-powered electrolysis with tandem cell photoelectrolysis", *ACS Energy Letters*, vol. 2, no. 1, pp. 45–51, 2016.

[5] A. Fujishima and K. Honda, "Electrochemical photolysis of water at a semiconductor electrode", *Nature*, vol. 238, no. 5358, pp. 37–38, 1972.

[6] S. Chu, W. Li, Y. Yan, T. Hamann, I. Shih, D. Wang, and Z. Mi, "Roadmap on solar water splitting: Current status and future prospects", *Nano Futures*, vol. 1, no. 2, p. 022 001, 2017.

[7] J. L. Young, M. A. Steiner, H. Döscher, R. M. France, J. A. Turner, and T. G. Deutsch, "Direct solar-to-hydrogen conversion via inverted metamorphic multijunction semiconductor architectures", *Nature Energy*, vol. 2, no. 4, p. 17 028, 2017.

[8] M. R. Nellist, F. A. Laskowski, F. Lin, T. J. Mills, and S. W. Boettcher, "Semiconductor–electrocatalyst interfaces: Theory, experiment, and applications in photoelectrochemical water splitting", *Accounts of chemical research*, vol. 49, no. 4, pp. 733–740, 2016.

[9] K. Takanabe, "Photocatalytic water splitting: Quantitative approaches toward photocatalyst by design", *ACS Catalysis*, vol. 7, no. 11, pp. 8006–8022, 2017.

[10] P. Lianos, "Production of electricity and hydrogen by photocatalytic degradation of organic wastes in a photoelectrochemical cell: The concept of the photofuelcell: A review of a re-emerging research field", *Journal of Hazardous Materials*, vol. 185, no. 2, pp. 575–590, 2011.

[11] D Sengupta, P Das, B Mondal, and K Mukherjee, "Effects of doping, morphology and film-thickness of photo-anode materials for dye sensitized solar cell application–a review", *Renewable and Sustainable Energy Reviews*, vol. 60, pp. 356–376, 2016.

[12] J. R. Swierk and T. E. Mallouk, "Design and development of photoanodes for water-splitting dye-sensitized photoelectrochemical cells", *Chemical Society Reviews*, vol. 42, no. 6, pp. 2357–2387, 2013.

[13] M. Vaelma, "Photodeposition of gold and platinum on titanium dioxide", Master's thesis, Aalto university, 2017.

[14] W. Schmickler and E. Santos, *Interfacial Electrochemistry*. Springer Berlin Heidelberg, 2010, ISBN: 9783642049378.

[15] J. Bisquert, A. Zaban, M. Greenshtein, and I. Mora-Seró, "Determination of rate constants for charge transfer and the distribution of semiconductor and electrolyte electronic energy levels in dye-sensitized solar cells by open-circuit photovoltage decay method", *Journal of the American Chemical Society*, vol. 126, no. 41, pp. 13 550–13 559, 2004.

[16] M. Grätzel, "Photoelectrochemical cells", *Nature*, vol. 414, no. 6861, p. 338, 2001.

[17] L. Ji, M. D. McDaniel, S. Wang, A. B. Posadas, X. Li, H. Huang, J. C. Lee, A. A. Demkov, A. J. Bard, J. G. Ekerdt, *et al.*, "A silicon-based photocathode for water reduction with an epitaxial $SrTiO_3$ protection layer and a nanostructured catalyst", *Nature nanotechnology*, vol. 10, no. 1, pp. 84–90, 2015.

[18] P. Cendula, S. D. Tilley, S. Gimenez, J. Bisquert, M. Schmid, M. Grätzel, and J. O. Schumacher, "Calculation of the energy band diagram of a photoelectrochemical water splitting cell", *The Journal of Physical Chemistry C*, vol. 118, no. 51, pp. 29 599–29 607, 2014.

[19] W. Gomes and F. Cardon, "Electron energy levels in semiconductor electrochemistry", *Progress in Surface Science*, vol. 12, no. 2, pp. 155–215, 1982.

[20] H. Reiss and A. Heller, "The absolute potential of the standard hydrogen electrode: A new estimate", *The Journal of Physical Chemistry*, vol. 89, no. 20, pp. 4207–4213, 1985.

[21] R. Ramette, "Outmoded terminology: The normal hydrogen electrode", *J. Chem. Educ*, vol. 64, no. 10, p. 885, 1987.

[22] E. Cohen, R. S. of Chemistry (Great Britain), I. U. of Pure, A. C. Physical, and B. C. Division, *Quantities, Units and Symbols in Physical Chemistry*. Royal Society of Chemistry, 2007, ISBN: 9780854044337.

[23] M. Archer and A. Nozik, *Nanostructured and Photoelectrochemical Systems for Solar Photon Conversion*, ser. Series on photoconversion of solar energy. Imperial College Press, 2008, ISBN: 9781860942556.

[24] R. Compton, *Electrode Kinetics: Reactions*, ser. Comprehensive Chemical Kinetics. Elsevier Science, 1987, ISBN: 9780080868219.

[25] R. Van de Krol and M. Grätzel, *Photoelectrochemical hydrogen production*. Springer, 2012, vol. 90.

[26] J. Li and N. Wu, "Semiconductor-based photocatalysts and photoelectrochemical cells for solar fuel generation: A review", *Catalysis Science & Technology*, vol. 5, no. 3, pp. 1360–1384, 2015.

[27] A. McNaught, A. Wilkinson, A. Jenkins, I. U. of Pure, and A. Chemistry, *IUPAC Compendium of Chemical Terminology: The Gold Book*. International Union of Pure and Applied Chemistry, 2006.

[28] C. Hu, *Modern Semiconductor Devices for Integrated Circuits*. Prentice Hall, 2010, ISBN: 9780136085256.

[29] E. L. Miller, "Solar hydrogen production by photoelectrochemical water splitting: The promise and challenge", in *On Solar Hydrogen & Nanotechnology*. John Wiley & Sons, Ltd, 2010, pp. 1–35, ISBN: 9780470823996.

[30] T. Ohta, *Solar-hydrogen energy systems: an authoritative review of water-splitting systems by solar beam and solar heat: hydrogen production, storage and utilisation*. Elsevier, 2013.

[31] R. Beranek, "(photo) electrochemical methods for the determination of the band edge positions of tio2-based nanomaterials", *Advances in Physical Chemistry*, vol. 2011, 2012.

[32] (2017, April 04). Reference solar spectral irradiance: Air mass 1.5, [Online]. Available: `http://rredc.nrel.gov/solar/spectra/am1.5/`.

[33] A. G. Scheuermann, J. P. Lawrence, K. W. Kemp, T Ito, A. Walsh, C. E. Chidsey, P. K. Hurley, and P. C. McIntyre, "Design principles for maximizing photovoltage in metal-oxide-protected water-splitting photoanodes", *Nature materials*, vol. 15, no. 1, pp. 99–105, 2016.

[34] L. Gao, Y. Cui, R. H. Vervuurt, D. van Dam, R. P. van Veldhoven, J. P. Hofmann, A. A. Bol, J. E. Haverkort, P. H. Notten, E. P. Bakkers, *et al.*, "High-efficiency inp-based photocathode for hydrogen production by interface energetics design and photon management", *Advanced functional materials*, vol. 26, no. 5, pp. 679–686, 2016.

[35] S. Rühle, "Tabulated values of the shockley–queisser limit for single junction solar cells", *Solar Energy*, vol. 130, pp. 139 –147, 2016, ISSN: 0038-092X.

[36] W. Shockley and H. J. Queisser, "Detailed balance limit of efficiency of p-n junction solar cells", *Journal of applied physics*, vol. 32, no. 3, pp. 510–519, 1961.

[37] R. van de Krol, Y. Liang, and J. Schoonman, "Solar hydrogen production with nanostructured metal oxides", *Journal of Materials Chemistry*, vol. 18, no. 20, pp. 2311–2320, 2008.

[38] M. F. Weber and M. Dignam, "Splitting water with semiconducting photoelectrodes—efficiency considerations", *International Journal of Hydrogen Energy*, vol. 11, no. 4, pp. 225–232, 1986.

[39] M. G. Walter, E. L. Warren, J. R. McKone, S. W. Boettcher, Q. Mi, E. A. Santori, and N. S. Lewis, "Solar water splitting cells", *Chemical reviews*, vol. 110, no. 11, pp. 6446–6473, 2010.

[40] M. Ni, M. K. Leung, D. Y. Leung, and K Sumathy, "A review and recent developments in photocatalytic water-splitting using TiO_2 for hydrogen production", *Renewable and Sustainable Energy Reviews*, vol. 11, no. 3, pp. 401–425, 2007.

[41] T Bak, J Nowotny, M Rekas, and C. Sorrell, "Photo-electrochemical hydrogen generation from water using solar energy. materials-related aspects", *International journal of hydrogen energy*, vol. 27, no. 10, pp. 991–1022, 2002.

[42] M. Barroso, S. R. Pendlebury, A. J. Cowan, and J. R. Durrant, "Charge carrier trapping, recombination and transfer in hematite (α-fe 2 o 3) water splitting photoanodes", *Chemical Science*, vol. 4, no. 7, pp. 2724–2734, 2013.

[43] A. Paracchino, N. Mathews, T. Hisatomi, M. Stefik, S. D. Tilley, and M. Grätzel, "Ultrathin films on copper (i) oxide water splitting photocathodes: A study on performance and stability", *Energy & Environmental Science*, vol. 5, no. 9, pp. 8673–8681, 2012.

[44] R. H. Coridan, A. C. Nielander, S. A. Francis, M. T. McDowell, V. Dix, S. M. Chatman, and N. S. Lewis, "Methods for comparing the performance of energy-conversion systems for use in solar fuels and solar electricity generation", *Energy & Environmental Science*, vol. 8, no. 10, pp. 2886–2901, 2015.

[45] L. Bertoluzzi, P. Lopez-Varo, J. A. J. Tejada, and J. Bisquert, "Charge transfer processes at the semiconductor/electrolyte interface for solar fuel production: Insight from impedance spectroscopy, supporting information", *Journal of Materials Chemistry A*, vol. 4, no. 8, pp. 2873–2879, 2016.

[46] T. J. Mills, F. Lin, and S. W. Boettcher, "Theory and simulations of electrocatalyst-coated semiconductor electrodes for solar water splitting", *Physical review letters*, vol. 112, no. 14, p. 148 304, 2014.

[47] J. Kierzenka and L. F. Shampine, "A BVP solver based on residual control and the matlab PSE", *ACM Transactions on Mathematical Software (TOMS)*, vol. 27, no. 3, pp. 299–316, 2001.

[48] ——, "A BVP solver that controls residual and error", *JNAIAM J. Numer. Anal. Indust. Appl. Math*, vol. 3, pp. 27–41, 2008.

[49] W. W. Gärtner, "Depletion-layer photoeffects in semiconductors", *Physical Review*, vol. 116, no. 1, p. 84, 1959.

[50] J Reichman, "The current-voltage characteristics of semiconductor-electrolyte junction photovoltaic cells", *Applied Physics Letters*, vol. 36, no. 7, pp. 574–577, 1980.

[51] S. D. Tilley, M. Cornuz, K. Sivula, and M. Grätzel, "Light-induced water splitting with hematite: Improved nanostructure and iridium oxide catalysis", *Angewandte Chemie*, vol. 122, no. 36, pp. 6549–6552, 2010.

[52] H. Dotan, K. Sivula, M. Grätzel, A. Rothschild, and S. C. Warren, "Probing the photoelectrochemical properties of hematite ($\alpha - Fe_2O_3$) electrodes using hydrogen peroxide as a hole scavenger", *Energy & Environmental Science*, vol. 4, no. 3, pp. 958–964, 2011.

[53] ZAHNER elektrik, "Thales 02: Basics and applications", 2008. [Online]. Available: `http://zahner.de/pdf/Basics_and_Applications.pdf`.

[54] I. Tamm, "Über eine mögliche art der elektronenbindung an kristalloberflächen", *Zeitschrift für Physik*, vol. 76, no. 11-12, pp. 849–850, 1932.

[55] T. J. Mills, F. A. Laskowski, C. Dette, M. R. Nellist, F. Lin, and S. W. Boettcher, "The role of surface states in electrocatalyst-modified semiconductor photoelectrodes: Theory and simulations", *arXiv preprint arXiv:1707.03112*, 2017.

[56] A. Karkri, M. Hadrami, M. Benaichi, and A. Chetouani, "Numerical modelling of degenerate and nondegenerate semiconductors with the fermi-dirac distribution", in *Electrical and Information Technologies (ICEIT), 2016 International Conference on*, IEEE, 2016, pp. 255–259.

[57] A. Berger and J. Newman, "An integrated 1-dimensional model of a photoelectrochemical cell for water splitting", *Journal of The Electrochemical Society*, vol. 161, no. 8, E3328–E3340, 2014.